

## Full length article

## In-plane characterization of structural and thermodynamic properties for steps at faceted chemically heterogeneous solid/liquid interfaces

Hongtao Liang <sup>a</sup>, Brian B. Laird <sup>b</sup>, Mark Asta <sup>c</sup>, Yang Yang <sup>a,\*</sup><sup>a</sup> Physics Department and State Key Laboratory of Precision Spectroscopy, School of Physical and Material Science, East China Normal University, Shanghai 200062, China<sup>b</sup> Department of Chemistry, University of Kansas, Lawrence, KS 66045, USA<sup>c</sup> Department of Materials Science and Engineering, UC Berkeley, Berkeley, CA 94720, USA

## ARTICLE INFO

## Article history:

Received 3 August 2017

Received in revised form

23 September 2017

Accepted 25 September 2017

Available online 28 September 2017

## Keywords:

Al-Pb alloys

Solid/liquid interface

Steps free energy

Interface structure

Molecular dynamics simulations

## ABSTRACT

We present a methodology for studying steps at faceted chemically heterogeneous solid/liquid interfaces, based on equilibrium molecular-dynamics simulations. The methodology is applied to a faceted Al(111)/Pb(liquid) interface (750 K, ambient pressure), yielding a direct calculation of step free energy and extensive atomic-scale characterization for the interfacial layer containing the step. We demonstrate the power spectrum of the equilibrium step fluctuations obeys the capillary wave theory, and the calculated step free energy is consistent with experimental measurement [Acta Mater 2001; 49:4259]. The step fluctuations are identified to be governed by the attachment/detachment limited kinetics. Furthermore, we characterize the step by calculating the in-plane profiles of density, concentration, potential energy, pressure components and stresses. The fundamental properties of interface solid and interface liquid extracted from the in-plane profiles show orders of magnitudes difference in comparing with those predicted from the bulk Al-Pb alloy phase diagram. Several excess step properties are also determined along with defining a generalized Gibbs dividing surface.

© 2017 Acta Materialia Inc. Published by Elsevier Ltd. All rights reserved.

## 1. Introduction

Steps play important roles in crystal morphology [1] and many interfacial processes, including surface roughening [2] and faceting transitions [3], the collective fluctuations among neighboring vicinal steps [4], layer-by-layer growth process in solidification from of the melt [5,6], as well as VLS nanowire growth [7] and homoepitaxial growth [8]. Thermodynamic and structural properties of the steps govern the nucleation rate and the island growth during crystallization [9–12]. In addition, they determine the magnitude of interfacial mass transport and the persistence probability of step fluctuations, which are necessary to precisely control nanostructure fabrication [13,14]. Understanding these one-dimensional defects, in terms of their fundamental properties, is crucial for developing theories of phase nucleation at interfaces.

A key property that governs all important processes mentioned above is the step free energy  $\gamma_{st}$ . Using classical capillary wave theory (CWT) for an atomically rough step [15–17], leads to a well-

known relationship for the power-spectrum of (step) interfacial fluctuations [17],

$$\langle |\hat{\xi}_q|^2 \rangle = \frac{k_B T}{L \bar{\gamma}_{st} q^2} \quad (1)$$

Here,  $\hat{\xi}_q$  is the Fourier amplitude of the step fluctuation with wave vector  $q$ .  $k_B$  is Boltzmann constant,  $T$  is temperature,  $L$  is the macroscopic step length and  $\bar{\gamma}_{st} = \gamma_{st} + \frac{\partial^2 \gamma_{st}}{\partial \theta^2}$  is the step stiffness (related to  $\gamma_{st}$ ) and  $\theta$  is an angle of the local step-edge normal relative to the linear step normal direction. This relationship forms the core of the capillary fluctuation method (CFM) for the step system and provides a route to the determination of  $\bar{\gamma}_{st}$ . Using high-resolution scanning tunneling microscopy (STM), or other microscopy techniques, the wave vector dependence of the step fluctuation power spectrum can be directly measured to extract  $\bar{\gamma}_{st}$ . Such measurements have been typically accompanied by a second experimental investigation of the equilibrium 2d surface island shape to further resolve the angular dependence of  $\gamma_{st}$  and back out the value of  $\gamma_{st}$  at certain points of the 2d island perimeter [18,19]. This methodology has been successfully

\* Corresponding author.

E-mail address: [yyang@phy.ecnu.edu.cn](mailto:yyang@phy.ecnu.edu.cn) (Y. Yang).

applied to the study of surface steps in Si [18] and various metals [19–23]. Intensive experimental studies have inspired a number of theoretical achievements [24–27] including a very recent thermodynamic formalism of the temperature dependence of surface step free energies by Freitas et al. [28]. Because of the inherent difficulty in characterizing the properties of the steps buried within solid/liquid interfaces, the fundamental understanding of the faceted solid/liquid interfacial steps remains less advanced. There have been a few experimental and simulation studies devoted to the investigations of  $\gamma_{st}$  at solid/liquid interfaces [29–32]; however, these studies provided only indirect measures of  $\gamma_{st}$ . At present, the only direct measurement has been achieved by employing molecular-dynamics (MD) simulation and CFM to determine  $\gamma_{st}$  of steps at high temperature faceted Si(111)/SiAl(l) interfaces [33]. To the best of the authors' knowledge, no direct calculation of  $\gamma_{st}$  has yet been published for steps at the solid/liquid interface between two bulk phases that exhibit nearly complete immiscibility - in other words, a chemically heterogeneous solid-liquid interface.

The present study is also motivated by a series of *in situ* transmission-electron-microscopy (TEM) studies by Dahmen et al. [29,34–37] of the equilibrium shape and Brownian motion of small liquid Pb inclusions embedded in an Al crystal matrix. These studies yield unique insights into the kinetic processes and thermodynamic properties governing the motion of inclusion facets (e.g., step nucleation on Al(111)/Pb(l)). In addition, MD-based studies have been applied to characterize the structural and thermodynamic properties of planar Al(s)/Pb(l) interfaces [38,39]. These previous investigations provide excellent background to undertake a more detailed study of solid/liquid interface steps in this model chemically heterogeneous system.

The goal of this paper is the application of atomistic simulation methods to investigate the atomic-scale structural and thermodynamic properties of interfacial steps. This work focuses primarily on the interface liquid (IL), interface solid (IS) and the step lines, which coexist within an interfacial monoatomic layer at the Al(111)/Pb(l) interface, a representative faceted chemically heterogeneous solid/liquid interface. The dynamical properties of step fluctuations are explored in greater detail than is possible through experimental studies and we identify the collective disordering of small Al clusters at step-edges as the primary kinetic source contributing to mass transport. We perform a thorough analysis of various properties of the coexistence layer through the calculation of profiles for density, concentration, potential energy, pressure components and stress as functions of the distance normal to the step-edge. These interfacial profiles provide a new level of understanding of the novel thermodynamical and mechanical conditions for solid/liquid interface step. The fundamental properties for IL and IS extracted from the in-plane profiles are significantly different from those predicted from the bulk phase diagram [40]. In addition to the profiles, we also apply the CFM method to the direct calculation of  $\gamma_{st}$  for the solid/liquid interfacial steps at Al(111)/Pb(l) interface. In addition to the step free energy, other step excess quantities (excess energy, excess stress, and excess Pb absorption) are calculated from the in-plane profiles. The methodology proposed here should be applicable to interfacial layers engaged in interfacial prefreezing transitions [41–43], and potentially extendable to the exploration of multi-complexion equilibria and 1d phase boundaries, among them at grain boundaries [44–50].

This work is organized as follows. In Sec.2 we review the detailed methods and protocols used for preparing and performing the MD simulations, as well as a description of the various calculation/analysis methods employed. The principal results are presented in Sec.3. Finally, in Sec.4 we summarize and conclude.

## 2. Methodology

All MD simulations are performed using LAMMPS [51] using a time step of 2.0 fs. Constant *NVT* and *NPT* MD simulations use a Nosé-Hoover thermostat (with a temperature of 750 K) and a thermostat relaxation time of 0.1 ps and, for *NPT*, an Anderson barostat with a relaxation time of 1.0 ps and a pressure of 1 bar. The forcefield used to model the Al-Pb alloy system is the glue-type many-body potential of Landa, et al. [40]. This potential has been shown to describe the (111) Al/Pb solid/liquid interface well, with a roughening transition temperature ( $T_r = 826(4)$  K) in excellent agreement with the experimental value of 823 K [39]. Both TEM experiments [29] and atomistic simulations [38,39], show the chemically heterogeneous Al(111)/Pb(l) fcc solid/liquid interface to be faceted between the melting point of Pb and the  $T_r$  with stable interface steps present at orientations vicinal to (111).

To study the thermodynamics and dynamics of interfacial steps in this system, we constructed, using MD techniques described in Refs. [5] and [38], a series of well-equilibrated Al(111)/Pb(l) interfaces, each with a single step in the periodic simulation box. The equilibrated interfaces were sampled using constant *NVT* MD for 25 million steps, recording 50,000 MD trajectories for the subsequent analysis. Eleven systems were employed, labeled as system A ... K, to investigate possible finite size effects in our calculations, as listed in Table 1. The two cross-sectional dimensions of the interface,  $L_x$  and  $L_y$ , range from 83 Å and 46 Å to 203 Å and 277 Å, respectively. The thickness (in the z direction) of the Al crystal slab,  $L_s$ , ranges from 28 Å to 127 Å. Also shown in Table 1 are the interfacial orientations and number of particles in each solid Al and liquid Pb sample. Fig. 1 (a) shows a representative snapshot of an equilibrated interface from one of the *NVT* simulations. For each interface simulation, we divided the total *NVT* trajectory into ten independent blocks for statistical averaging. Each simulation contains two independent solid/liquid interfacial steps giving a total of twenty independent samples to determine statistical uncertainty.

The interfacial monoatomic layer containing the step and both solid and liquid terraces were extracted using information from the fine-scaled density profile across each Al(111)/Pb(l) interface studied. In Fig. 1 (b), which shows the Al and Pb density profiles for system C, the Pb and Al density peaks at the interface overlap, corresponding to the Al step and the adjacent liquid terrace within the monoatomic layer. For each recorded MD configuration as shown in Fig. 1 (a), all Al and Pb particles located between the neighboring density minima of the interfacial Al and Pb peaks were defined to form the interfacial layer. The positions of the density minima,  $z_i^*$  and  $z_j^*$ , are shown as dashed lines. Fig. 1 (c) shows a snapshot of the extracted interfacial monoatomic layer. To

**Table 1**  
Interfacial orientations, cross-sectional dimensions, crystal slab thickness and number of solid and liquid atoms in each of the interfacial systems studied.

| ID | Orientation | $L_x$ (Å) | $L_y$ (Å) | $L_s$ (Å) | $N_s$  | $N_l$ |
|----|-------------|-----------|-----------|-----------|--------|-------|
| A  | (29,28,29)  | 143       | 46        | 70        | 27272  | 14611 |
| B  | (17,16,17)  | 83        | 80        | 70        | 27716  | 14865 |
| C  | (29,28,29)  | 143       | 80        | 70        | 47725  | 25541 |
| D  | (41,40,41)  | 203       | 80        | 70        | 67679  | 36227 |
| E  | (29,28,29)  | 143       | 104       | 70        | 61361  | 32844 |
| F  | (29,28,29)  | 143       | 127       | 70        | 74997  | 40171 |
| G  | (29,28,29)  | 143       | 196       | 70        | 115904 | 62017 |
| H  | (29,28,29)  | 143       | 277       | 70        | 163632 | 89267 |
| I  | (17,16,17)  | 83        | 80        | 28        | 11692  | 14865 |
| J  | (17,16,17)  | 83        | 80        | 56        | 22692  | 14865 |
| K  | (17,16,17)  | 83        | 80        | 127       | 50111  | 14865 |

**Table 2**

Thermodynamic parameters extracted from an equilibrium Al(111)/Pb(l) interface with a single step (system D), under 750 K and 1 bar. Superscript “s” and “l” stand for (bulk or interface) solid and liquid. **Bulk phases:**  $X_{\text{Pb}}^s$  and  $X_{\text{Al}}^l$  are the coexistence mutual-miscibilities;  $\rho$  and  $\rho_e$  are the particle number density and the potential energy density;  $p_{11}$ ,  $p_{22}$  and  $p_{33}$  are the pressure components. **IS and IL:**  $\bar{X}_{\text{Pb}}^s$ ,  $\bar{X}_{\text{Al}}^l$ ,  $\bar{\rho}$ ,  $\bar{p}_{11}$ ,  $\bar{p}_{22}$  and  $\bar{p}_{33}$ . **Interface excesses:**  $\tau$ ,  $e^{\text{Al}}$  and  $\Gamma_{\text{Pb}}^{\text{Al}}$  are the interfacial excesses of stress, energy and number of Pb atoms. **Step excesses:**  $\bar{\tau}$ ,  $\bar{e}^{\text{Al}}$  and  $\bar{\Gamma}_{\text{Pb}}^{\text{Al}}$ . Error bars in parentheses represent 95% confidence intervals on the last digit(s) shown.

| $X_{\text{Pb}}^s$       | $X_{\text{Al}}^l$       | $\rho^s$         | $\rho^l$         | $\rho_e^s \cdot 10^{-10}$        | $\rho_e^l \cdot 10^{-10}$       | $p_{11,22}^s$       | $p_{11,22}^l$       | $p_{33}^s$       | $p_{33}^l$       | $\tau$       | $e^{\text{Al}}$                  | $\Gamma_{\text{Pb}}^{\text{Al}}$       |
|-------------------------|-------------------------|------------------|------------------|----------------------------------|---------------------------------|---------------------|---------------------|------------------|------------------|--------------|----------------------------------|--|
| %                       | %                       | $\text{nm}^{-3}$ | $\text{nm}^{-3}$ | $(\text{J} \cdot \text{m}^{-3})$ |                                 |                     |                     | (kbar)           |                  |              | $(\text{J} \cdot \text{m}^{-2})$ | $\text{\AA}^{-2}$                      |
| 0                       | 0.12 (1)                | 58.654 (3)       | 30.986 (3)       | -3.0624 (3)                      | -0.9309 (2)                     | 0.007 (9)           | 0.002 (13)          | 0.001 (7)        | 0.001 (9)        | 0.524 (3)    | 0.89 (1)                         | -0.0173 (3)                            |
| $\bar{X}_{\text{Pb}}^s$ | $\bar{X}_{\text{Al}}^l$ | $\bar{\rho}^s$   | $\bar{\rho}^l$   | $\bar{\rho}_e^s \cdot 10^{-10}$  | $\bar{\rho}_e^l \cdot 10^{-10}$ | $\bar{p}_{11,22}^s$ | $\bar{p}_{11,22}^l$ | $\bar{p}_{33}^s$ | $\bar{p}_{33}^l$ | $\bar{\tau}$ | $\bar{e}^{\text{Al}}$            | $\bar{\Gamma}_{\text{Pb}}^{\text{Al}}$ |
| %                       | %                       | $\text{nm}^{-3}$ | $\text{nm}^{-3}$ | $(\text{J} \cdot \text{m}^{-3})$ |                                 |                     |                     | (kbar)           |                  |              | $(\text{J} \cdot \text{m}^{-2})$ | $\text{\AA}^{-2}$                      |
| 2.0 (4)                 | 20 (4)                  | 55 (1)           | 36 (3)           | -2.68 (3)                        | -1.20 (10)                      | -8.32 (8)           | -7.13 (5)           | -9.14 (16)       | -1.77 (10)       | 0.09 (2)     | 1.2 (5)                          | -0.025 (8)                             |

distinguish IS from IL and to locate the positions of the steps at the faceted solid/liquid interface, we employed a structural order parameter [52] to classify all particles within the extracted layer as either solid or liquid. The extracted layer was subdivided into  $m$  discrete strips of width  $\lambda = 1.444 \text{ \AA}$  along the direction parallel to the step ( $y$  axis). We then defined the instantaneous step position ( $\xi$ ) for each strip based on the order parameter distribution. The instantaneous coarse-grained step shape was then defined by  $\xi(y_i)$ , with  $y_i = (i - 0.5)\lambda$ ,  $i = 1 \sim m$ . More details, about the interface construction, as well as the protocol for locating the interfacial layer and the step, can be found in Section S1 of the Supplemental Information [53].

Knowledge of the time evolution of the step position function  $\xi(y)$  can be used to directly calculate the relaxation times for step fluctuations, the step stiffness, as well as to provide an assessment of the validity of classical CWT in the solid/liquid interfacial step system. In addition, the extractions of the interfacial monoatomic layers enable us to carry out a high quality and reliable statistical

characterization of various structural and thermodynamic properties of the IL and IS, and the step boundary between them. We have calculated from the trajectories a number of interfacial profiles to show the change in specific properties as a function of  $x^*$ . These calculations consist of both fine-scale and coarse-scaled profiles, in which, the fine-scale profiles were determined by binning the simulation box in  $x^*$  and averaging the quantity of interest within each bin, and the coarse-scaled profiles were determined from the fine-scale profiles using a finite-impulse-response (FIR) smoothing algorithm [54]. In addition, two sets of fundamental parameters describing IL and IS properties and a few step excess quantities were determined, based on the coarse-scaled profiles described above. The details for these measurements are as follows:

- a) **Step fluctuation spectrum, step stiffness and step free energy:** Using the time evolution of  $\xi(y_i)$  from simulation output, autocorrelation functions of the step fluctuation amplitudes were calculated as [1,55],

$$C_q(t) = A_n \langle \hat{\xi}_q(t) \hat{\xi}_{-q}(0) \rangle, \quad (2)$$

where  $A_n$  is the normalizing constant. The calculated  $C_q(t)$  were fitted to  $\exp(-t/\tau_q)$  to measure the relaxation times  $\tau_q$  for different wave vectors  $q$ .  $\tau_q(t)$  should scale as  $1/q^2$  if the step fluctuation rate-limiting mechanism is attachment/detachment,  $1/q^3$  if the diffusion of the atoms on the terrace are rate-limiting, or  $1/q^4$  for diffusion along the step-edge [1]. We also calculated the time-averaged power spectrum of the capillary fluctuations from which the interfacial stiffness,  $\bar{\gamma}_{\text{st}}$ , was determined using Eq. (1) from a weighted least-squares linear regression of a log-log plot of  $\langle |\hat{\xi}_q|^2 \rangle$  versus  $q$ . As will be presented below, the fluctuation spectra of the Al(111)/Pb(l) interfacial steps at 750 K are well predicted by Eq. (1), indicating that CFM is applicable to the calculation of the step stiffness for chemically heterogeneous faceted solid/liquid interfaces. In addition, we have carried out independent long-time MD simulations of 2d islands within Al(111)/Pb(l) interfaces and characterized the equilibrium 2d island shape with sufficient statistical quality [53]. To estimate  $\gamma_{\text{st}}$  we used a relationship,  $\gamma_{\text{st}} = \bar{\gamma}_{\text{st}} R_m \kappa_m$ , proposed by Giesen et al. [19], based on the fact that 2d island in equilibrium has a constant chemical potential related to  $\bar{\gamma}_{\text{st}}$  and the local curvature at any point on its perimeter. The subscript ‘m’ indicates the point of minimum curvature on the perimeter,  $R$  and  $\kappa$  are the radius and curvature at that point.

- b) **Density profiles:** The in-plane mean Al and Pb density profiles,  $\bar{\rho}_{\text{Al}}(x^*)$  and  $\bar{\rho}_{\text{Pb}}(x^*)$ , were calculated by binning the interfacial monoatomic layer in the  $x^*$  direction using a bin size of  $\Delta x^* = 0.05 \text{ \AA}$ . The density profile was then calculated from the binned data

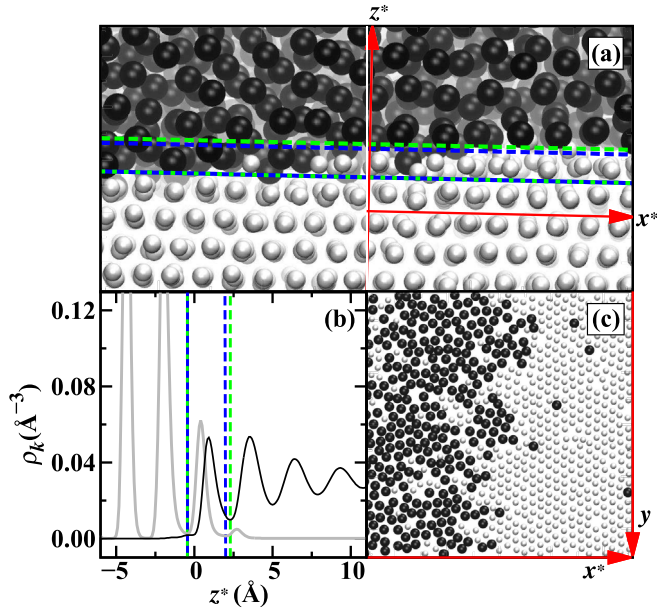


**Fig. 1.** (a) Snapshot of Al(111)/Pb(l) interface with single  $[10\bar{1}]$  step (a portion of system C). The viewpoint defined by the direction perpendicular to the page is  $[10\bar{1}]$  (or  $y$ ). The vicinal normal is  $[29,28,29]$  (or  $z$ ).  $x^*$  and  $z^*$  axes are defined as  $[\bar{1}2\bar{1}]$  and  $[111]$  directions, perpendicular to the step. Pb particles are shown as dark grey spheres and have larger size, while light grey smaller spheres represent Al particles. (b) Fine-scaled Al (light grey) and Pb (dark grey) density profiles [38] for the Al(111)/Pb(l) interface. Zero point ( $z^*$  axis) in corresponding to the Gibbs Dividing Surface, chosen as the interfacial excess of Al atoms equals to zero. Dashed lines show the locations of the interfacial layer. (c) Plan view of an extracted interfacial layer.

$$\tilde{\rho}_k(x^*) = \frac{\langle N_{x^*}^k \rangle}{L_y \Delta x^* \delta z^*}, \quad (3)$$

where  $N_{x^*}^k$  is the number of particles of type  $k$  ( $k = \text{Al}, \text{Pb}$ ) between  $x^* - \Delta x^*/2$  and  $x^* + \Delta x^*/2$  at time  $t$ ,  $\langle \dots \rangle$  denotes for the time-average.  $\delta z^*$  is the thickness of the interfacial layer (defined as the distance between the minima of the density peaks at the interface in Fig. 1). The  $x^*$  coordinates used in this profile and the subsequent profiles listed below were measured relative the generalized Gibbs dividing surface defined below.

c) **Concentration profiles:** The coarse-scaled density profiles were used to determine the in-plane concentration profiles, as follows

$$\tilde{X}_k(x^*) = \frac{\tilde{\rho}_k(x^*)}{\tilde{\rho}_{\text{Al}}(x^*) + \tilde{\rho}_{\text{Pb}}(x^*)}. \quad (4)$$

d) **Potential energy profiles:** The in-plane potential energy profiles were calculated by averaging the potential energy for atom  $k$  type ( $U_{x^*}^k$ ) in discrete bins and dividing by the volume of the bins,

$$\tilde{\rho}_{e,k}(x^*) = \frac{\langle U_{x^*}^k \rangle}{L_y \Delta x^* \delta z^*}. \quad (5)$$

e) **Pressure profiles:** For the particles located between  $z_i^*$  and  $z_f^*$ , the fine-scaled pressure tensors (components) were calculated as the sum of the ideal gas pressure and the excess pressure determined based on the virial theorem, in each discrete bins. The in-plane pressure components profiles were calculated as,

$$\tilde{P}_{mn}(x^*) = \frac{\langle \frac{1}{3} \sum_{j=1}^{N_{x^*}} M_j v_{jm} v_{jn} \rangle + \langle \sum_{j=1}^{N_{x^*}} r_{jm} f_{jn} \rangle}{L_y \Delta x^* \delta z^*}, \quad (6)$$

$m$  and  $n$  are taken from the set of cartesian directions  $\{x^*, y$  and  $z^*\}$  (hereafter referred as  $\{1, 2$  and  $3\}$  for simplicity). The summations run over  $j$ th atom of the  $N_{x^*}$  atoms in the discrete bin with a volume  $L_y \Delta x^* \delta z^*$ .  $M$  is mass.  $v$ ,  $r$  and  $f$  are the velocity, position and force vector of atom  $j$ , respectively.

f) **Interfacial stress profile:** The interface stress  $S$  is defined as the difference between two pressure components normal and parallel to the Al(111)/Pb(l) interface. Here, we concentrated on interface layer, as defined above, calculated as a function of  $x^*$ , rather than of  $z^*$ , as is the usual case:

$$S(x^*) = \tilde{p}_{33}(x^*) - \frac{1}{2} [\tilde{p}_{11}(x^*) + \tilde{p}_{22}(x^*)]. \quad (7)$$

g) **Lateral stress profile for the steps:** We define the in-plane step lateral stress  $\tilde{S}$  as the difference between the pressure components normal and parallel to the interfacial step:

$$\tilde{S}(x^*) = \tilde{p}_{11}(x^*) - \tilde{p}_{22}(x^*). \quad (8)$$

h) **Fundamental parameters for IS and IL:** The volume densities of the IS and IL, labeled as  $\tilde{\rho}^s$  and  $\tilde{\rho}^l$  were extracted from the in-plane total (Al and Pb) density profile by averaging over

approximately one-third of the coarse-scaled bins in the middle of IS and IL. Other properties calculated in this study include mutual miscibilities,  $\tilde{X}_{\text{Al}}^l$  and  $\tilde{X}_{\text{Pb}}^s$ ; average potential energy per unit volume,  $\tilde{\rho}_e^l$  and  $\tilde{\rho}_e^s$ ; pressure components,  $\tilde{p}_{11}^s, \tilde{p}_{11}^l, \tilde{p}_{22}^s, \tilde{p}_{22}^l, \tilde{p}_{33}^s, \tilde{p}_{33}^l$ . The full set of these calculated properties of interest for IL and IS were used to compare with those for the bulk phases of Al-Pb alloy, determined from a set of coarse-scaled interfacial profiles [53].

i) **Excess step properties:** Generally, excess interfacial properties can be defined for an interfacial system by first defining a so-called Gibbs Dividing Surface (GDS), which is an imaginary surface exactly partitioning the interfacial system into volume regions corresponding to the two phases separated by the interface. In this view, the interfacial excess of a particular extensive property is obtained by calculating the value of the property for the full interfacial system minus the value of the property calculated as if the partitioned volumes take on their representative bulk values up to the dividing surface. This difference is then divided by the interfacial area to give the interfacial excess. For the interfacial plane, in which two “semi-2d phases” (IL and IS) coexist and form a semi-1d defect (step), we follow Frolov and Mishin [46], and introduce a GDS to separate IL and IS “phases”. This surface, which is normal to the Al(111)/Pb(l) interface and parallel to the step, is set at a position ( $x_{\text{GDS}}^*$ ) such that the step excess number of Al particles is equal to zero [38], that is,

$$\tilde{\Gamma}_{\text{Al}} = \frac{\tilde{N}_{\text{Al}}}{L_{x^*} \delta z^*} - \tilde{\rho}_{\text{Al}}^l L_{x^*}^l - \tilde{\rho}_{\text{Al}}^s L_{x^*}^s = 0 \quad (9)$$

where  $\tilde{N}_{\text{Al}}$  is mean total number of particles of Al in the interfacial layer,  $\tilde{\rho}_{\text{Al}}^s$  and  $\tilde{\rho}_{\text{Al}}^l$  are the volume densities of Al for IS and IL, respectively,  $L_{x^*}^l$  and  $L_{x^*}^s$  are the  $x^*$ -direction lengths of IL and IS defined by the dividing plane and  $L_{x^*}$  is the sum of the two lengths. Once the GDS is set, the step excess of the extensive quantity  $\tilde{Y}$ , for the in-plane IL-IS coexistence is defined as:

$$\tilde{y}_{\text{excess}} = \frac{\tilde{Y}}{L_{x^*} \delta z^*} - \tilde{y}^l L_{x^*}^l - \tilde{y}^s L_{x^*}^s \quad (10)$$

where  $\tilde{y}^l$  and  $\tilde{y}^s$  are the volume densities of the quantities  $\tilde{Y}$  in the IL and IS, respectively. Three step excesses were calculated, the excess energy,  $\tilde{e}^{\text{Al}}$ , the excess stress,  $\tilde{\tau}$ , and the excess number of Pb atoms,  $\tilde{\Gamma}_{\text{Pb}}^{\text{Al}}$ . The superscript “Al” denotes that these quantities are calculated using a dividing plane where the excess number of Al atoms is zero. The calculated step excesses were compared with the corresponding Al(111)/Pb(l) interfacial excesses ( $\tau$ ,  $e^{\text{Al}}$ ,  $\Gamma_{\text{Pb}}^{\text{Al}}$ ), at the same temperature.

### 3. Results and discussion

#### 3.1. In-plane step geometries and fluctuation kinetics

After 50 ns of  $Np_zAT$  MD simulation, the Al(111)/Pb(l) interfaces reach equilibrium in both structure and concentration. Fig. 2 (a)–(c) show a series of snapshots of the interfacial monoatomic layer shown in Fig. 1 (b) separated by 1.0 ps. The atoms are color coded based on the values of the order parameter,  $\psi(i)$ : blue for IS and green for IL. A few vacancies and Pb impurities (interstitial) are found in IS. In the IL side, Al appears in the form of single atoms or small clusters, uniformly dissolved in IL to form a binary solution. The step positions  $\xi(y_i)$ , determined from discretized strips, are

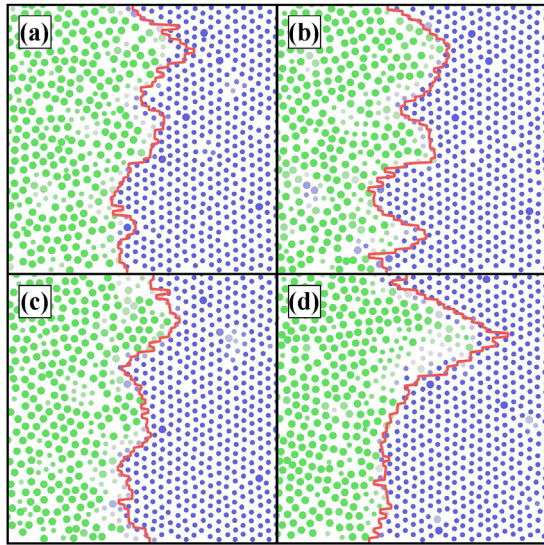


**Fig. 2.** Snapshots of Al(111)/Pb(l) interfacial layers representing IL-IS coexistence.  $T = 750$  K. Al and Pb particles are represented with smaller and larger circular discs, and are color coded based on the order-parameter value: blue for IS and green for IL. The calculated step positions  $\xi(y_i)$  are plotted as red solid lines. Frames (a), (b) and (c) show successive trajectories with a 1ps time interval, whereas, (d) captures a configuration in which a large Al cluster loses crystalline order. An animation of the step fluctuation can be found in the [Supplemental Material \[53\]](#). (For interpretation of the references to colour in this figure legend, the reader is referred to the web version of this article.)

represented by a thick solid line, which could well separate IL from IS. Its rugged shape indicates the step is rough, without evident kinks or noticeable overhangs along the step-edge.

By examining the successive time evolution of the step-edges, we find two distinct modes of mass transport. i) Many small clusters of Al particles in the same vicinity, randomly lose their crystalline order and transform back to the crystalline phase. Such frequent processes (picosecond timescale) are associated with Al-Pb inter-diffusion and inter-mixing at step-edges. For example, [Fig. 2](#) (d) captures an Al cluster consisting of about 30 noncrystalline particles, elongating the step. ii) Sometimes the small clusters are detaching away from the step-edge into the IL, and sometimes rejoining the solid terrace.

To distinguish the limiting kinetics that governing the step fluctuations, we have calculated the autocorrelation functions [53] of the step fluctuation amplitudes  $C_q(t)$  and measured the relaxation times  $\tau_q$  as a function of the wave vector  $q$ , for system D. Within the  $q$  range as shown in [Fig. 3](#) (a),  $\tau_q(q)$  fits well to a power law ( $\sim 1/q^{n_k}$ ) with the fitted exponent  $n_k = 2.1(1)$ , consistent with that expected for a attachment/detachment limited kinetics ( $\sim 1/q^2$ ). The fluctuation mode with smallest  $q$  has longest relaxation time ( $\sim 700$ ps) that limit the statistics for its sampling in the MD simulations.

### 3.2. Step stiffness, free energy

[Fig. 3](#) (b) shows the power spectrum of the equilibrium step fluctuations on a log-log scale, where the amplitudes of the fluctuation spectra  $\langle |\hat{\xi}_q|^2 \rangle$  are scaled by the step lengths,  $L_y$ . The scaling line with the slope of  $-2$  predicted by Eq. (1), is observed to hold for  $q$  over a wide range ( $q_1 = 2\pi/L_y < q < \sim 0.5 \text{ \AA}^{-1}$ ) for all Al(111)/Pb(l) interfaces studied. There are observed leveling off at lower wave vectors is most likely due to the extremely long equilibration and sampling time (comparing 50 ns) associated with these long-

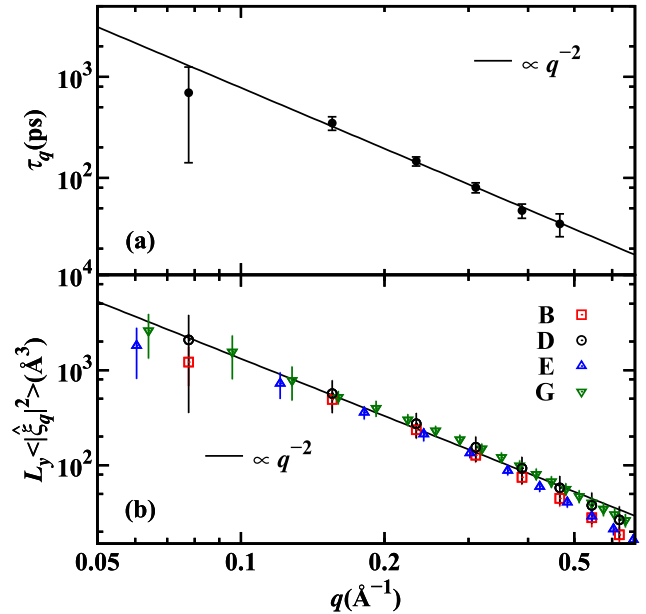


**Fig. 3.** (a) The relaxation times  $\tau_q$ , determined by fitting the amplitude autocorrelation functions  $C_q(t)$  to  $\exp(-t/\tau_q)$  are shown as a function of the wave vector  $q$ , system D. A  $1/q^2$  scaling represents attachment/detachment limited step fluctuation kinetics is shown as the solid line. (b) Log-log plot of the power spectra of equilibrium fluctuations (scaled with  $L_y$ ) for steps at the Al(111)/Pb(l) interfaces (four selected systems plotted),  $T = 750$  K. The solid line indicates the theoretical slope of  $-2$ .

wavelength modes. If one were to extend the simulations substantially longer, these data should also agree with the  $1/q^2$  trend. At larger  $q$ , the power spectrum shows sub- $1/q^2$  behavior, corresponding to length scales where the continuum description of CWT breaks down. The threshold value ( $\sim 0.5 \text{ \AA}^{-1}$ ) where the deviation occurs is well below the upper wave vector limit  $q_m$  (wavelength on the order of the molecular diameter) and is dependent upon the details of the calculation of the step-edge position  $\xi(y_i)$ . In determining  $\bar{\gamma}_{st}$ , we performed weighted least-squares fits of  $\ln(L_y \langle |\hat{\xi}_q|^2 \rangle)$  versus  $\ln(q)$ , using the data for values of  $q$  ranging between  $q_1$  and  $0.5 \text{ \AA}^{-1}$ .

To assess finite size effects, we have calculated  $\bar{\gamma}_{st}$  for a variety of different values of  $L_x$ ,  $L_y$  and  $L_s$ . The data show that  $\bar{\gamma}_{st}$  is constant (within statistical error) over the values of  $L_x$  and  $L_s$  examined, leading us to conclude that the system sizes in these two directions are outside the finite size scaling regime, given our resolution - see [Fig. 4](#) (a) and (b). There is, however, a weak, but significant dependence on  $L_y$  - see [Fig. 4](#) (c), which is likely due to changes in configurational entropy associated with step fluctuations as functions of step length [56]. To determine the infinite size limit, we approach this data in two ways. One way would be to assume that  $\bar{\gamma}_{st}$  is an analytic function of  $1/L_y$  and expand about  $1/L_y = 0$  in a Taylor Series. To test this, we first fit the first 4 points in [Fig. 4](#) (c) using linear weighted least squares regression in  $1/L_y$ . This gives a limiting ( $1/L_y = 0$ ) value of  $65(13) \times 10^{-10} \text{ mJ/m}$  for  $\bar{\gamma}_{st}$ . Fitting the entire data set in [Fig. 4](#) (c) using quadratic and cubic weighted least squares regression gives nearly identical values of  $64(11) \times 10^{-10} \text{ mJ/m}$  and  $67(10) \times 10^{-10} \text{ mJ/m}$ , respectively. These fits are shown as lines in [Fig. 4](#) (c). The raw data and the fitting functions shown in [Fig. 4](#) are given in the [Supplemental Information \[53\]](#).

The equilibrium shapes of 2d islands within Al(111)/Pb(l) interfaces were calculated from independent MD simulations [53]. As shown in [Fig. 5](#), they are found to be perfectly matching circles. Within statistical uncertainties, the radii along the island perimeter

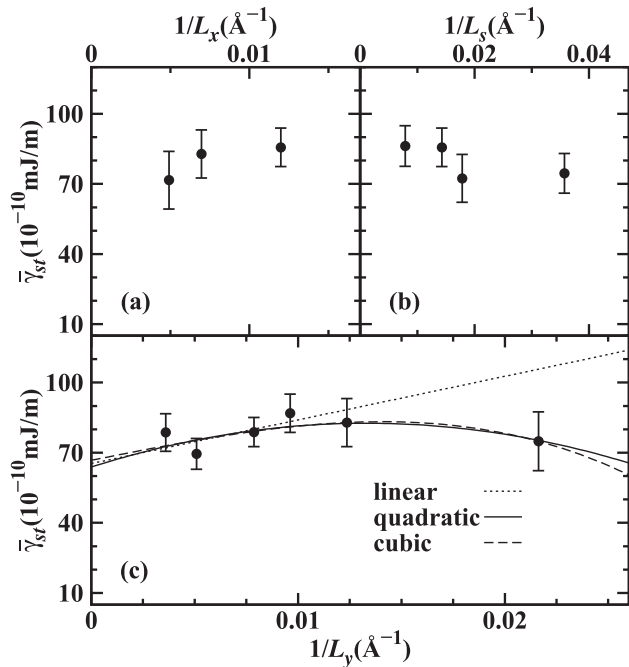


**Fig. 4.** (a)  $\bar{\gamma}_{st}$  as a function of  $1/L_x$ , at fixed  $L_y$  and  $L_s$  (system B, C, D). (b)  $\bar{\gamma}_{st}$  as a function of  $1/L_s$ , at fixed  $L_x$  and  $L_y$  (system B, I–K). (c)  $\bar{\gamma}_{st}$  as a function of  $1/L_y$ , at fixed  $L_x$  and  $L_s$  (system A, C, E–H). Lines represent the weighted least-squares fits to linear, quadratic and cubic functions.

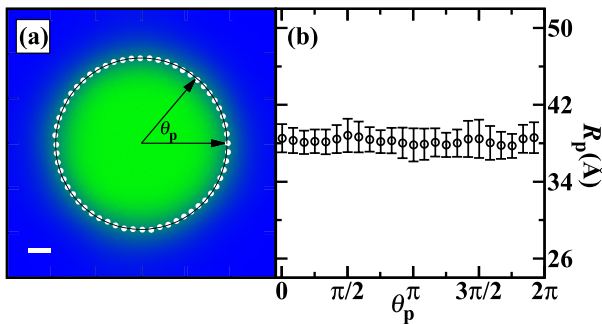


**Fig. 5.** (a) Density contour map and the coarse-grained outline for the 2d liquid island in Al(111)/Pb(l) interface at 750 K. The shape outline is represented with white discs. The solid line is fitted to a circle. Scale bar 1 nm. (b) Radius along the island perimeter  $R_p$  as a function of angular directions  $\theta_p$ , error bars represent 95% confidence intervals estimated from statistical average.

are identical, so that  $R_m \kappa_m \approx 1.0$ , thus  $\gamma_{st} \approx \bar{\gamma}_{st}$ . This implies that the free energy of the Al(111)/Pb(l) interfacial steps is isotropic at 750 K.

In a TEM experimental study on the equilibrium shape of liquid Pb inclusions within Al matrix by Gabrisch et al. [29], a step free energy at 350 °C (623 K) was estimated to be  $\gamma_{st} = 190 \times 10^{-10}$  mJ/m. This step free energy decreased with increasing temperature linearly up to the roughening transition temperature at 550 °C (823 K), at which point the step free energy vanishes. A linear interpolation of the experimental data to 750 K produces an estimated value for  $\gamma_{st}$  of  $69 \times 10^{-10}$  mJ/m, which is in excellent agreement with the macroscopic value of  $\gamma_{st}$  predicted from our calculations. Dividing  $\gamma_{st}$  by the (111) inter-planar distance  $d_{[111]} = 2.35878$  Å, we obtain the perimeter free energy  $\gamma_p = 27(5)$  mJ/m<sup>2</sup>, a quantity that has the same units as the interfacial free energies. Mullins and Rohrer [57] suggested that the interfacial free energy to perimeter free energy ratio is valuable for

understanding the limiting facet nucleation size during the equilibrium shape changes in faceted crystal particles or cavities. The experimental value of the Al(111)/Pb(l) interfacial free energy  $\gamma_{sl}$  is 419 mJ/m<sup>2</sup> (623 K [58], slightly above the melting point of Pb), and the liquid/liquid interfacial free energy  $\gamma_{ll}$  is 126 mJ/m<sup>2</sup> at 922.4 K near melting point of Al [59], no data for  $\gamma_{sl}$  is available at 750 K. However, according to free energies quoted above, we estimate that  $\gamma_p$  is approximately an order of magnitude smaller than  $\gamma_{sl}$ .

### 3.3. Atomistic characterization of the in-plane IL-IS coexistence

Now we turn to detailed in-plane structural characterizations for the interfacial monoatomic layer. All the profiles shown below are calculated from a representative system using a bin size of 0.05 Å and averaging over 50000 snapshots. The position of the GDS corresponds to zero point of the horizontal axis,  $x^* > 0$  for IS and  $x^* < 0$  for IL.

A closeup of the fine-scaled variation of the densities ( $\tilde{\rho}_{Al}$  and  $\tilde{\rho}_{Pb}$ ) is shown in Fig. 6 (a). The plots show the variations in the densities for each component species and the rapid oscillations in IS correspond to the spatial periodicities of the surface crystalline Al atoms. Similarly, the relatively uniform profile corresponds to IL (Pb). The Al density (gray line) oscillations dampen gradually toward the IL as the step is traversed along the  $x^*$  axis. This decay spans over a length scale of roughly 13–15 surface lattice spacings and transforms into a corrugated flat profile with density value slightly above zero in the IL. This length scale is in contrast to the case of a rough type heterogeneous solid/liquid interface [38,41,42,60], in which the solid density decays over a length scale of only 5–6 lattice spacings and terminates at the liquid surface. The relatively large decay length shown in the plot can be attributed to the noticeable capillary waves along the step-edges and the low values of  $\gamma_{st}$ . The weak residual density peaks in the first interfacial liquid layer have been reported as the modulation by the underlying Al crystal structure [38]. The corrugated Al density peaks in IL, consistent with the Al crystal lattice, can be attributed

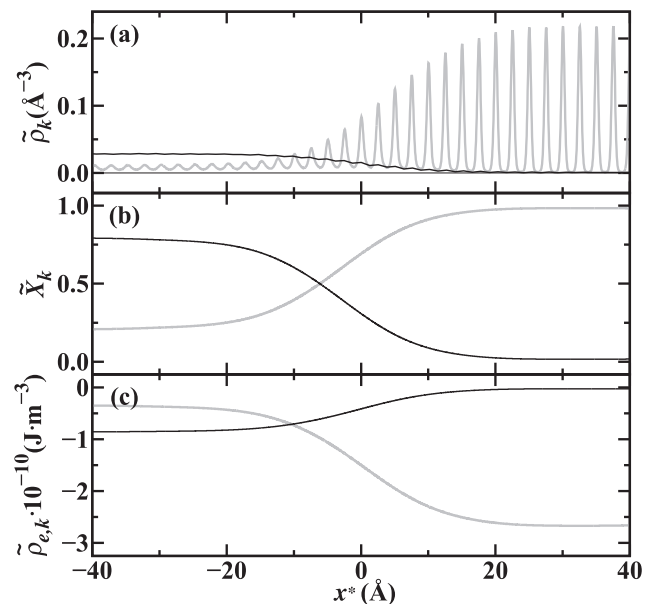


**Fig. 6.** In-plane fine-scaled density (a), coarse-scaled concentration (b) and potential energy (c) profiles across the IL-IS coexistence line within Al(111)/Pb(l) interface (system D). The lines in dark and light gray represent properties for Pb and Al, respectively. The zero point of  $x^*$  corresponding to the GDS is chosen so that the step excess of Al atoms equals to zero.

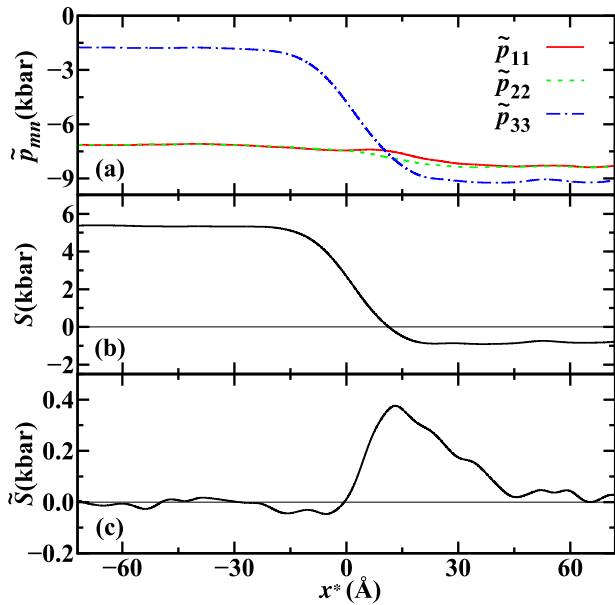


**Fig. 7.** In-plane coarse-scaled pressure components (a), interfacial stress (b) and step lateral stress (c) profiles across the IL-IS coexistence line within Al(111)/Pb(l) interface (system D). The zero point of  $x^*$ , corresponding to the GDS, is chosen such that the step excess of Al atoms equals to zero.

to the competition between the kinetic trapping of Al atoms at binding sites provided by the substrate crystalline plane and their disordering diffusion driven by the surrounding liquid Pb atoms. The Pb density (black line) does not contain any remarkable density oscillations compared with heterogeneous solid/liquid interfaces, in which liquid in contact with the solid surfaces can exhibit layer ordering in terms of significant density peaks [38,41,42,60]. This difference may due to the capillary wave fluctuations broadening the IL-IS transition region and washing out the intrinsic structure.

Complementing the information provided by the oscillatory fine-scaled density profiles are the coarse-scaled concentration and potential-energy profiles plotted in Fig. 6 (b) and (c). The profiles flatten out far away from the GDS and correspond to the “bulk” parts of the IL and IS. The calculated equilibrium solubility of Pb in IS and Al in IL are  $\bar{X}_{\text{Pb}}^l = 0.02(4)$  and  $\bar{X}_{\text{Al}}^l = 0.2(4)$ , listed in Table 2, showing a large increase of two orders of magnitude compared with corresponding values of  $X_{\text{Pb}}^l$  and  $X_{\text{Al}}^l$  for bulk phases of Al-Pb alloy. More fundamental parameters extracted from the coarse-scaled in-plane density and potential energy profiles are also listed in Table 2 -these show only small differences from their bulk values.

As expected, the calculated pressure components in bulk solid and bulk liquid,  $p_{mn}^s$  and  $p_{mn}^l$ , are all equal to ambient pressure within the statistical uncertainty (see in Table 2), indicating that the two bulk phases are in mechanical equilibrium [53]. However, the in-plane pressure components for the interfacial layer ( $z_i^* < z^* < z_f^*$ ), which are plotted in panel (a) of Fig. 7, represent an entirely different mechanical picture. All three in-plane pressure components profiles show significant negative pressure, with absolute values at least three orders of magnitude larger than the ambient pressure of the bulk phases. The profiles exhibit nonuniform features across the IL-IS coexistence line, different from the pressure profiles across the solid/liquid interfaces. The  $\tilde{p}_{11}$  and  $\tilde{p}_{22}$  components listed in Table 2 share the same values (within statistical uncertainties) of around -8.3 kbar and -7.1 kbar for IS and IL, respectively. However, the values of  $\tilde{p}_{33}$  for IS and IL are about -9.1 kbar and -1.8 kbar,

both values are different from those of  $\tilde{p}_{11}$  and  $\tilde{p}_{22}$ . From IL to IS, the pressure components all decay over the same length scale of about 40 Å into states under lower pressures, the  $\tilde{p}_{33}(x^*)$  shows a more remarkable decrease in comparison with the other two components. The profiles in Fig. 7 (a) demonstrate the IL-IS coexistence, within an equilibrium faceted heterogeneous solid/liquid interface, is under non-hydrodynamic environment and possesses significant anisotropy and heterogeneity among the pressure components.

The stress profile  $S(z^*)$  measures the difference between the longitudinal and transverse average pressures across the solid/liquid interface. Fig. 7 (b) monitors the in-plane 2d distribution of  $S$  for the interfacial layer ( $z_i^* < z^* < z_f^*$ ). The values of  $S$  for both IL and IS are far from 0 kbar. From IL to IS,  $S$  decays from 5.4 kbar to -0.82 kbar in the similar fashion as the in-plane density/concentration profiles. The change in the sign of  $S$ , laterally, is unexpected, because only a few studies uncovered the longitudinal stress variation coupling with sign changes at solid/liquid interfaces [38,41,42,54,61]. The positive sign in the region  $x^* < -20$  Å suggesting that IL is under lateral tension, whereas the opposing IS is under lateral compression (negative stress). The overall magnitude and sign of the interfacial stress for the entire interfacial monolayer with the step is a hybrid result, a nearly linear combination of tensile or compressive states in the coexisting IL and IS, based upon the allocation of the two “semi-2d phases”. For example, system B has a greater proportion of IL than system D, leading to,  $S = 4.5$  kbar for the interfacial monoatomic layer of B is larger than  $S = 3.0$  kbar for D.

The in-plane step lateral stress  $\tilde{S}$  profile is plotted in Fig. 7 (c). For a properly equilibrated solid/liquid interface, the stress in the 3d bulk solid and bulk liquid is zero due to the hydrostatic balance condition. The profile shows zero  $\tilde{S}$  in both IL and IS and a single positive peak, lies on the position of about 12 Å to the right of the GDS. The positive sign in  $\tilde{S}$  suggesting that IS near step is in a state of lateral stretching. At this position, the frequent attachment/detachment of small Al clusters along the step-edge occurs, which could be responsible for stretching the step and giving rise to the semi-1d tensile state along the step-edge.

The calculated interfacial and step excess stresses (for system D),  $\tau$  and  $\tilde{\tau}$  in Table 2, are 0.524(3) and 0.09(2) J·m<sup>-2</sup>, respectively. The positive signs originate primarily from the tensile states of the bulk (or interface) solid Al adjacent to GDS of the interface (or step). The magnitude of  $\tau$  is about six times larger than  $\tilde{\tau}$ , similar to the magnitude difference between the interfacial free energy and the perimeter free energy above. We found the value of  $\tau$  depends on the number of the steps rather than the system sizes. For an equilibrium Al(111)/Pb(l) interface without steps, we obtained a value of  $\tau = 0.515(4)$  J·m<sup>-2</sup>, slightly lower than values of  $\tau$  for currently studied interfacial systems with one single step. System B has much smaller  $L_x$  yet a greater proportion of IL than system D, however,  $\tau$  for system B (0.523(3) J·m<sup>-2</sup>) is identical to that for system D. Unfortunately, there has been no fundamental theory that could accurately predict interfacial or step stresses even on a qualitative level.

In contrast to the excess stresses, both excess energies and excess number of Pb atoms, as listed in Table 2, for the solid/liquid interface and the IL-IS coexistence step share the same sign and the similar magnitude. In principle, we could use the calculated step excesses and the value of  $\gamma_{\text{st}}$  at 750 K, and extend the Gibbs-Cahn integration formalism for surface steps [28] to current case of solid/liquid interfacial steps, to determine the step free energies over the entire temperature range from the freezing point of Pb up to the roughening transition temperature. In practice, however, such calculations of the step free energies would be extremely

challenging due to the large computational effort required to calculate excess properties at the many temperature grid points required for the integration and due to the difficulties in accurately calculating the chemical potential difference between the Al and Pb species, which would require additional semi-grand canonical Monte Carlo simulations.

#### 4. Summary

We presented a methodology for the calculation of structural and thermodynamic properties for steps at faceted chemically heterogeneous solid/liquid interfaces. The methodology makes use of equilibrium molecular-dynamics (MD) simulations, calculates the step free energy, and characterizes the in-plane distribution profiles of various fundamental parameters for the IL-IS coexistence with the interfacial layer. This methodology was applied to the faceted Al(111)/Pb(l) interface at 750 K.

We demonstrated that the instantaneous structure of the step is rough, and the power spectra of the equilibrium step fluctuations obey classical CWT remarkably well. The attachment/detachment of clusters of Al atoms via collective disordering or drifting motions were identified in the mass transport during the step fluctuation. In addition, we have measured fluctuation relaxation times as functions of wave vector and found they are consistent with  $1/q^2$  scaling, corresponding to step fluctuation kinetics limited by attachment/detachment processes along the step-edges. We examined the equilibrium shape of the 2d island within Al(111)/Pb(l) interfaces with adequate statistics and proved that the step free energy  $\gamma_{st}$  is isotropic. The finite-size scaling of  $\bar{\gamma}_{st}$  (or  $\gamma_{st}$ ) with respect to system sizes, *i.e.*,  $L_x$ ,  $L_y$  and  $L_s$ , were discussed in detail. A weak size dependence of the data on  $L_y$  was noticed. We extracted the limiting values of the  $\bar{\gamma}_{st}$  (or  $\gamma_{st}$ ) in the limit of the infinite step length, yielding excellent agreement with the experimental result.

The two sets of fundamental parameters for IL and IS, extracted from the in-plane profiles, were found to be dramatically different from each other. Several parameters (such as mutual-miscibilities) in both sets show orders of magnitude difference compared with bulk phases. More interestingly, our analysis demonstrated that IL and IS are coexist under negative local pressures. Also demonstrated is the in-plane coexistence of the tensile and compressive state within the faceted solid/liquid interfaces. In addition, three excess step properties were calculated based on defining a generalized Gibbs dividing surface. Various properties calculated for the IL-IS coexistence are essential to the development of a detailed thermodynamic theory for faceted (heterogeneous) solid/liquid interfaces.

#### Acknowledgements

The authors would like to gratefully acknowledge Ulrich Dahmen (Lawrence Berkeley National Laboratory), De-yan Sun (East China Normal University) and Xin-gao Gong (Fudan University) for helpful discussions and suggestions. BBL acknowledges funding from the National Science Foundation [Grant No. CHE-1465226]. MA acknowledge funding from the National Science Foundation [Grants Nos. DMR-1105409 and DMR-1507033]. YY acknowledge funding from the Chinese National Science Foundation [Grant No. 11504110], 111 Project [Grant No. B12024] and Large Instruments Open Foundation of ECNU.

#### Appendix A. Supplementary data

Supplementary data related to this article can be found at <https://doi.org/10.1016/j.actamat.2017.09.059>.

#### References

- [1] H.-C. Jeong, E.D. Williams, Steps on surfaces: experiment and theory, *Surf. Sci. Rep.* 34 (68) (1999) 171–294, [https://doi.org/10.1016/S0167-5729\(98\)00010-7](https://doi.org/10.1016/S0167-5729(98)00010-7).
- [2] A.A. Chernov, Roughening and melting of crystalline surfaces, *Prog. Cryst. Growth Charact. Mater.* 26 (1993) 195–218, [https://doi.org/10.1016/0960-8974\(93\)90015-V](https://doi.org/10.1016/0960-8974(93)90015-V).
- [3] J.B. Hannon, N.C. Bartelt, B.S. Swartzentruber, J.C. Hamilton, G.L. Kellogg, Step faceting at the (001) surface of boron doped silicon, *Phys. Rev. Lett.* 79 (1997) 4226–4229, <https://doi.org/10.1103/PhysRevLett.79.4226>.
- [4] T. Ihle, C. Misbah, O. Pierre-Louis, Equilibrium step dynamics on vicinal surfaces revisited, *Phys. Rev. B* 58 (1998) 2289–2309, <https://doi.org/10.1103/PhysRevB.58.2289>.
- [5] D. Buta, M. Asta, J. J. Hoyt, Kinetic coefficient of steps at the Si(111) crystal-melt interface from molecular dynamics simulations, *J. Chem. Phys.* 127(7), <https://doi.org/10.1063/1.2754682>.
- [6] P. Saidi, J. Hoyt, Atomistic simulation of the step mobility at the AlSi(111) crystal-melt interface using molecular dynamics, *Comput. Mater. Sci.* 111 (2016) 137–147, <https://doi.org/10.1016/j.commatsci.2015.09.040>.
- [7] S.H. Oh, M.F. Chisholm, Y. Kauffmann, W.D. Kaplan, W. Luo, M. Rühle, C. Scheu, Oscillatory mass transport in vapor-liquid-solid growth of sapphire nanowires, *Science* 330 (6003) (2010) 489–493, <https://doi.org/10.1126/science.1190596>.
- [8] M. Giesen, H. Ibach, Homoepitaxial growth on nominally flat and stepped Cu(111) surfaces: island nucleation in fcc sites vs. hcp stacking fault sites, *Surf. Sci.* 529 (12) (2003) 135–143, [https://doi.org/10.1016/S0039-6028\(03\)00077-3](https://doi.org/10.1016/S0039-6028(03)00077-3).
- [9] R.S. Wagner, W.C. Ellis, Vaporliquid-solid mechanism of single crystal growth, *Appl. Phys. Lett.* 4 (5) (1964) 89–90, <https://doi.org/10.1063/1.1753975>.
- [10] A. Chernov, Notes on interface growth kinetics 50 years after burton, Cabrera and Frank, *J. Cryst. Growth* 264 (4) (2004) 499–518, <https://doi.org/10.1016/j.jcrysgro.2003.12.076> proceedings of the Symposium - Progress in Crystal Growth.
- [11] A. A. Golovin, S. H. Davis, P. W. Voorhees, Step-flow growth of a nanowire in the vapor-liquid-solid and vapor-solid-solid processes, *J. Appl. Phys.* 104(7), <https://doi.org/10.1063/1.2977729>.
- [12] C.-Y. Wen, J. Tersoff, K. Hillerich, M.C. Reuter, J.H. Park, S. Kodambaka, E.A. Stach, F.M. Ross, Periodically changing morphology of the growth interface in Si, Ge, and gap nanowires, *Phys. Rev. Lett.* 107 (2011) 025503, <https://doi.org/10.1103/PhysRevLett.107.025503>.
- [13] Z. Toroczka, E.D. Williams, Nanoscale fluctuations at solid surfaces, *Phys. Today* 52 (12) (1999) 24–28, <https://doi.org/10.1063/1.882897>.
- [14] D.B. Dougherty, I. Lyubintsev, E.D. Williams, M. Constantin, C. Dasgupta, S.D. Sarma, Experimental persistence probability for fluctuating steps, *Phys. Rev. Lett.* 89 (2002) 136102, <https://doi.org/10.1103/PhysRevLett.89.136102>.
- [15] F.P. Buff, R.A. Lovett, F.H. Stillinger, Interfacial density profile for fluids in the critical region, *Phys. Rev. Lett.* 15 (1965) 621–623, <https://doi.org/10.1103/PhysRevLett.15.621>.
- [16] J.D. Weeks, Structure and thermodynamics of the liquid-vapor interface, *J. Chem. Phys.* 67 (7) (1977) 3106–3121, <https://doi.org/10.1063/1.435276>.
- [17] M.P.A. Fisher, D.S. Fisher, J.D. Weeks, Agreement of capillary-wave theory with exact results for the interface profile of the two-dimensional Ising model, *Phys. Rev. Lett.* 48 (1982) 368, <https://doi.org/10.1103/PhysRevLett.48.368>.
- [18] N.C. Bartelt, R.M. Tromp, E.D. Williams, Step capillary waves and equilibrium island shapes on Si(001), *Phys. Rev. Lett.* 73 (1994) 1656–1659, <https://doi.org/10.1103/PhysRevLett.73.1656>.
- [19] M. Giesen, C. Steimer, H. Ibach, What does one learn from equilibrium shapes of two-dimensional islands on surfaces? *Surf. Sci.* 471 (13) (2001) 80–100, [https://doi.org/10.1016/S0039-6028\(00\)00888-8](https://doi.org/10.1016/S0039-6028(00)00888-8).
- [20] D.C. Schlöfner, L.K. Verheij, G. Rosenfeld, G. Comsa, Determination of step free energies from island shape fluctuations on metal surfaces, *Phys. Rev. Lett.* 82 (1999) 3843–3846, <https://doi.org/10.1103/PhysRevLett.82.3843>.
- [21] C. Steimer, M. Giesen, L. Verheij, H. Ibach, Experimental determination of step energies from island shape fluctuations: a comparison to the equilibrium shape method for Cu(100), Cu(111), and Ag(111), *Phys. Rev. B* 64 (2001) 085416, <https://doi.org/10.1103/PhysRevB.64.085416>.
- [22] S. Dieluweit, H. Ibach, M. Giesen, T.L. Einstein, Orientation dependence of the Cu(001) surface step stiffness: failure of solid-on-solid and Ising models to describe experimental data, *Phys. Rev. B* 67 (2003) 121410, <https://doi.org/10.1103/PhysRevB.67.121410>.
- [23] J. Ikononov, K. Starbova, H. Ibach, M. Giesen, Measurement of step and kink energies and of the step-edge stiffness from island studies on Pt(111), *Phys. Rev. B* 75 (2007) 245411, <https://doi.org/10.1103/PhysRevB.75.245411>.
- [24] M. Holzer, M. Wortis, Low-temperature expansions for the step free energy and facet shape of the simple-cubic Ising model, *Phys. Rev. B* 40 (1989) 11044–11058, <https://doi.org/10.1103/PhysRevB.40.11044>.
- [25] S. Kodiyalam, K.E. Khor, N.C. Bartelt, E.D. Williams, S. Das Sarma, Energetics of vicinal Si(111) steps using empirical potentials, *Phys. Rev. B* 51 (1995) 5200–5213, <https://doi.org/10.1103/PhysRevB.51.5200>.
- [26] T.J. Stasevich, H. Gebremariam, T.L. Einstein, M. Giesen, C. Steimer, H. Ibach, Low-temperature orientation dependence of step stiffness on 111 surfaces, *Phys. Rev. B* 71 (2005) 245414, <https://doi.org/10.1103/PhysRevB.71.245414>.
- [27] H.J. Zandvliet, Step free energy of an arbitrarily oriented step on a rectangular

- lattice with nearest-neighbor interactions, *Surf. Sci.* 639 (2015) L1–L4, <https://doi.org/10.1016/j.susc.2015.04.015>.
- [28] R. Freitas, T. Frolov, M. Asta, Step free energies at faceted solid surfaces: theory and atomistic calculations for steps on the Cu(111) surface, *Phys. Rev. B* 95 (2017) 155444, <https://doi.org/10.1103/PhysRevB.95.155444>.
- [29] H. Gabrisch, L. Kjeldgaard, E. Johnson, U. Dahmen, Equilibrium shape and interface roughening of small liquid Pb inclusions in solid Al, *Acta Mater.* 49 (20) (2001) 4259–4269, [https://doi.org/10.1016/S1359-6454\(01\)00307-X](https://doi.org/10.1016/S1359-6454(01)00307-X).
- [30] H. Ibach, M. Giesen, W. Schmickler, Potential dependence of the step line tension on surfaces in contact with an electrolyte, *J. Electroanal. Chem.* 544 (2003) 13–23, [https://doi.org/10.1016/S0022-0728\(03\)00055-X](https://doi.org/10.1016/S0022-0728(03)00055-X).
- [31] G. Beltramo, H. Ibach, M. Giesen, A novel approach to measure the step line tension and the step dipole moment on vicinal Au(001) electrodes, *Surf. Sci.* 601 (8) (2007) 1876–1885, <https://doi.org/10.1016/j.susc.2007.02.012>.
- [32] T. Frolov, M. Asta, Step free energies at faceted solid-liquid interfaces from equilibrium molecular dynamics simulations, *J. Chem. Phys.* 137(21), <https://doi.org/10.1063/1.4769381>.
- [33] P. Saidi, R. Freitas, T. Frolov, M. Asta, J. Hoyt, Free energy of steps at faceted (111) solid-liquid interfaces in the Si-Al system calculated using capillary fluctuation method, *Comput. Mater. Sci.* 134 (2017) 184–189, <https://doi.org/10.1016/j.commatsci.2017.03.044>.
- [34] E. Johnson, M.T. Levinsen, S. Steenstrup, S. Prokofjev, V. Zhilin, U. Dahmen, T. Radetic, One-dimensional random walk of nanosized liquid Pb inclusions on dislocations in Al, *Philos. Mag.* 84 (25–1) (2004) 2663–2673, <https://doi.org/10.1080/14786430410001671412>.
- [35] E. Johnson, S.I. Prokofjev, V.M. Zhilin, U. Dahmen, Diffusional behavior of nanoscale lead inclusions in crystalline aluminum, *Z. für Met.* 96 (10) (2005) 1171–1180, <https://doi.org/10.3139/146.101158>.
- [36] S.I. Prokofjev, V.M. Zhilin, E. Johnson, U. Dahmen, In situ electron microscopy study of the thermal motion of liquid lead nanoparticles in thin aluminum foils, *Bull. Russ. Acad. Sci. Phys.* 71 (12) (2007) 1662–1666, <https://doi.org/10.3103/S1062873807120039>.
- [37] T. Radetic, E. Johnson, D. Olmsted, Y. Yang, B. Laird, M. Asta, U. Dahmen, Step-controlled brownian motion of nanosized liquid Pb inclusions in a solid Al matrix, *Acta Mater.* 141 (2017) 427–433, <https://doi.org/10.1016/j.actamat.2017.09.040>.
- [38] Y. Yang, D.L. Olmsted, M. Asta, B.B. Laird, Atomistic characterization of the chemically heterogeneous AlPb solid-liquid interface, *Acta Mater.* 60 (12) (2012) 4960–4971, <https://doi.org/10.1016/j.actamat.2012.05.016>.
- [39] Y. Yang, M. Asta, B.B. Laird, Solid-liquid interfacial premelting, *Phys. Rev. Lett.* 110 (2013) 096102, <https://doi.org/10.1103/PhysRevLett.110.096102>.
- [40] A. Landa, P. Wynblatt, D. Siegel, J. Adams, O. Mryasov, X.-Y. Liu, Development of glue-type potentials for the AlPb system: phase diagram calculation, *Acta Mater.* 48 (8) (2000) 1753–1761, [https://doi.org/10.1016/S1359-6454\(00\)00002-1](https://doi.org/10.1016/S1359-6454(00)00002-1).
- [41] J.P. Palafox-Hernandez, B.B. Laird, M. Asta, Atomistic characterization of the Cu-Pb solid-liquid interface, *Acta Mater.* 59 (8) (2011) 3137–3144, <https://doi.org/10.1016/j.actamat.2011.01.053>.
- [42] J.P. Palafox-Hernandez, B.B. Laird, Orientation dependence of heterogeneous nucleation at the CuPb solid-liquid interface, *J. Chem. Phys.* 145 (21) (2016) 211914, <https://doi.org/10.1063/1.4962424>.
- [43] D.T. Limmer, Interfacial ordering and accompanying divergent capacitance at ionic liquid-metal interfaces, *Phys. Rev. Lett.* 115 (2015) 256102, <https://doi.org/10.1103/PhysRevLett.115.256102>.
- [44] W.D. Kaplan, D. Chatain, P. Wynblatt, W.C. Carter, A review of wetting versus adsorption, complexions, and related phenomena: the Rosetta Stone of wetting, *J. Mater. Sci.* 48 (17) (2013) 5681–5717, <https://doi.org/10.1007/s10853-013-7462-y>.
- [45] P.R. Cantwell, M. Tang, S.J. Dillon, J. Luo, G.S. Rohrer, M.P. Harmer, Grain boundary complexions, *Acta Mater.* 62 (2014) 1–48, <https://doi.org/10.1016/j.actamat.2013.07.037>.
- [46] T. Frolov, Y. Mishin, Phases, phase equilibria, and phase rules in low-dimensional systems, *J. Chem. Phys.* 143(4), <https://doi.org/10.1063/1.4927414>.
- [47] T. Frolov, M. Asta, Y. Mishin, Segregation-induced phase transformations in grain boundaries, *Phys. Rev. B* 92 (2015) 020103, <https://doi.org/10.1103/PhysRevB.92.020103>.
- [48] N. Zhou, J. Luo, Developing grain boundary diagrams for multicomponent alloys, *Acta Mater.* 91 (2015) 202–216, <https://doi.org/10.1016/j.actamat.2015.03.013>.
- [49] T. Frolov, M. Asta, Y. Mishin, Phase transformations at interfaces: observations from atomistic modeling, *Curr. Opin. Solid State Mater. Sci.* (2016), <https://doi.org/10.1016/j.cossms.2016.05.003>.
- [50] G.S. Rohrer, The role of grain boundary energy in grain boundary complexion transitions, *Curr. Opin. Solid State Mater. Sci.* 20 (5) (2016) 231–239, <https://doi.org/10.1016/j.cossms.2016.03.001>.
- [51] S. Plimpton, Fast parallel algorithms for short-range molecular dynamics, *J. Comput. Phys.* 117 (1) (1995) 1–19, <https://doi.org/10.1006/jcph.1995.1039>.
- [52] J.R. Morris, Complete mapping of the anisotropic free energy of the crystal-melt interface in Al, *Phys. Rev. B* 66 (2002) 144104, <https://doi.org/10.1103/PhysRevB.66.144104>.
- [53] In-plane characterization of structural and thermodynamic properties for steps at faceted chemically heterogeneous solid/liquid interfaces. [Supplementary Material].
- [54] R.L. Davidchack, B.B. Laird, Simulation of the hard-sphere crystal-melt interface, *J. Chem. Phys.* 108 (22) (1998) 9452–9462, <https://doi.org/10.1063/1.476396>.
- [55] R. Freitas, T. Frolov, M. Asta, Capillary Fluctuations of Surface Steps: an Atomistic Simulation Study for the Model Cu(111) System. arXiv:1706.03110.
- [56] M.P. Gelfand, M.E. Fisher, Finite-size effects in fluid interfaces, *Phys. A Stat. Mech. its Appl.* 166 (1) (1990) 1–74, [https://doi.org/10.1016/0378-4371\(90\)90099-E](https://doi.org/10.1016/0378-4371(90)90099-E).
- [57] W.W. Mullins, G.S. Rohrer, Nucleation barrier for volume-conserving shape changes of faceted crystals, *J. Am. Ceram. Soc.* 83 (1) (2000) 214–216, <https://doi.org/10.1111/j.1151-2916.2000.tb01173.x>.
- [58] M. Mclean, The kinetics of spheroidization of lead inclusions in aluminium, *Philos. Mag.* 27 (6) (1973) 1253–1266, <https://doi.org/10.1080/14786437308226884>.
- [59] W. Hoyer, I. Kaban, M. Merkwitz, Liquid-liquid interfacial tension in immiscible binary Al-based alloys, *J. Opt. Adv. Mat.* 5 (2003) 1069.
- [60] P. Geysersmans, D. Gorse, V. Pontikis, Molecular dynamics study of the solid-liquid interface, *J. Chem. Phys.* 113 (15) (2000) 6382–6389, <https://doi.org/10.1063/1.1290730>.
- [61] T. Frolov, Y. Mishin, Orientation dependence of the solid-liquid interface stress: atomistic calculations for copper, *Model. Simul. Mater. Sci. Eng.* 18 (7) (2010) 074003, <https://doi.org/10.1088/0965-0393/18/7/074003>.

# Supplemental Information for “In-plane Characterization of Structural and Thermodynamic Properties for the Steps at Faceted Chemically Heterogeneous Solid/Liquid Interfaces”

Hongtao Liang<sup>1</sup>, Brian B. Laird<sup>2</sup>, Mark Asta<sup>3</sup>, Yang Yang<sup>1,\*</sup>

<sup>1</sup> *Physics Department and State Key Laboratory of Precision Spectroscopy, School of Physical and Material Science, East China Normal University, Shanghai 200062, China*

<sup>2</sup> *Department of Chemistry, University of Kansas, Lawrence, KS 66045, USA*

<sup>3</sup> *Department of Materials Science and Engineering, UC Berkeley, Berkeley, CA 94720, USA*

\* Author to whom correspondence should be addressed: [yyang@phy.ecnu.edu.cn](mailto:yyang@phy.ecnu.edu.cn)

## Table of Contents

- **Section S1. Supporting Information of MD Simulation Details**
  - A. Solid sample with single stepped vicinal surface
  - B. Construction of the equilibrium solid/liquid interface
  - C. Locating interfacial layer and an animation of the extracted monolayer
  - D. Step positions
- **Section S2. Supporting Information of Step Fluctuations and Step Free Energy Calculation**
  - A. Supporting data: Al(111)/Pb(*l*) interfacial step free energy
  - B. Amplitude autocorrelation function
  - C. Equilibrium island shape at Al(111)/Pb(*l*) interface
- **Section S3. Supporting Information of the In-Plane Characterization**
  - A. In-plane structure of IS and IL at Al(111)/Pb(*l*)
  - B. Supporting data:  $\tilde{X}_{\text{Al}}^l$  and  $\tilde{X}_{\text{Pb}}^s$
  - C. Coarse-scaled interfacial profiles for 750K Al(111)/Pb(*l*)

## SECTION S1. SUPPORTING INFORMATION OF MD SIMULATION DETAILS

### A. Solid sample with single stepped vicinal surface

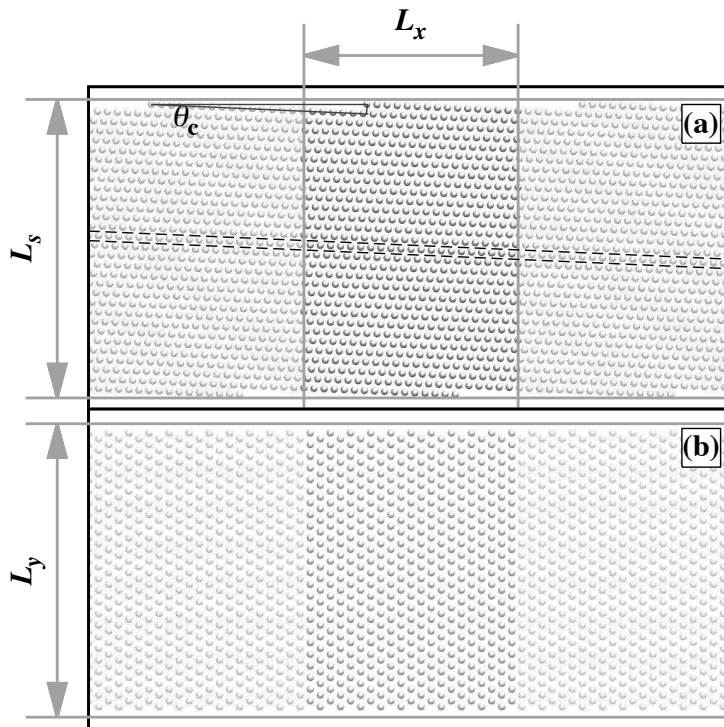


Fig. S 1. (a) Construction of a fcc crystal block with vicinal surface containing a single step. The side view of such block construction, together with its periodic images (lighter color), provide a simulation model of a vicinal surface which its plane indices (11 10 11).  $\theta_c$  refers to the angle between [111] and [11 10 11]. Two of the surfaces (top and bottom) created are normal to  $z$  axis. (b) In-plane view of an atomic layer in the bulk part of the crystal, which is labeled by the parallel dashed lines in panel (a). To produce a perfect match to the fcc lattice across the periodic boundaries, the value of  $L_x$  needs to be strictly obeying Eq.S1.

The technique of constructing vicinal interfaces in the current study was introduced by Buta et al.[1] in the study of interfacial kinetics of crystallization of silicon. This technique has advantages in that it reduce the system sizes without breaking the periodic boundary condition. Theoretically, steps on fcc (111) surface could exit along two main directions,  $[10\bar{1}]$  or  $[\bar{1}2\bar{1}]$ .

We use periodic boundary condition in a direction along the step, *i.e.*  $[10\bar{1}]$  direction for  $y$  axis in the simulation box. Similarly, the treatment on the creation of the simulation box on  $x$  axis also requires careful considerations.

Besides the periodic boundary condition in  $y$ , one could easily create a periodic crystal block with (111) plane normal to  $z$  axis of the simulation box, with two parallel surface steps on the solid terrace along  $x$  axis. As discussed in Ref.2, the two steps also have slightly different structures. Unfortunately, the simulations based on this type of construction may present a non-negligible step-step interaction that is harmful to the measurement of  $\gamma_{st}$ , especially for the step systems with very large capillary fluctuations. We have found that the intensity and frequency of the step fluctuation are much larger than those in the vicinal surface systems with single step because the dissolved Al atoms at step-edges diffuse across the liquid regime, the smaller the step-step distance is, the more effective step-step interactions show up. We found for the largest system size we could reasonably perform in this study,  $L_x = 200\text{\AA}$ , the step-step interaction is still evident under this type of construction.

To solve this problem, we adopt a vicinal surface construction in which we create a single step on one surface within a periodic box. The distance between two steps is  $L_x$ , nearly twice as large as the step-step distance in the previous construction, with an identical number of atoms. To achieve this under periodic boundary condition along  $x$ , we must rotate the crystal by  $\theta_c$  around  $[10\bar{1}]$ , clockwise or anti-clockwise and simultaneously apply a well defined  $L_x$  so that the stacking sequence within the simulation box is commensurate with its periodic images. The length  $L_s$  along  $z$  is constrained to trim crystal surface and produce a single step on the vicinal surface.

In this study, we rotate the crystal anti-clockwise around  $[10\bar{1}]$ , the crystal orientation along  $z$  axis is changed from  $[111]$  to  $[hkl]$ . Note that, for a rotation around  $[10\bar{1}]$ , the indices  $h$  and  $l$  are equal, and  $\theta_c = \arccos[(h+k+l)/\sqrt{3(h^2+k^2+l^2)}]$ . The periodic boundary condition along  $x$  for vicinal surface construction requires constraints that (i) periodic length in  $x$ ,  $L_x^2 = d_{[111]}^2 + \delta_{[\bar{1}2\bar{1}]}^2$  and (ii)  $\tan \theta_c = d_{[111]}/\delta_{[\bar{1}2\bar{1}]}$ , in which,  $d_{[111]} = \frac{\sqrt{3}}{3}a_{Al}$  is the distance between fcc (111) planes,  $\delta_{[\bar{1}2\bar{1}]} = m\frac{\sqrt{6}}{2}a_{Al} + \frac{\sqrt{6}}{6}a_{Al}$  corresponds to the projection of  $L_x$  on  $[\bar{1}2\bar{1}]$ ,  $m$  is an integer relating to the number of unit cells of the constructed system box.

Finally, the simplified form of the constraints is given by  $k = m = h - 1$ ,  $l = h$  and

$$L_x = a_{\text{Al}} \sqrt{\frac{3}{2}h^2 - 2h + 1}, \quad (\text{S1})$$

this periodic length gives a single step on the vicinal surface ( $hkh$ ). Fig.S1 illustrates such construction in detail.

## B. Construction of the equilibrium solid/liquid interface

The complete process can be described as follows:

i) Samples of solid Al were prepared by trimming a bulk Al ideal fcc crystal lattice at 750K to form simulation boxes with dimensions  $L_x \times L_y \times L_s$ . The lattice constant of Al  $a_{\text{Al}} = 4.08553\text{\AA}$ . The box dimensions  $L_x$  and  $L_y$  were chosen strictly to ensure that the trimmed solid Al satisfies the periodic boundary conditions, while the choice of  $L_s$  validate two vicinal interfaces (upper and lower) with a single step with its boundary alongs  $[10\bar{1}]$  or  $y$  axis in the simulation box. Our choice of the interface orientations (vicinal norms), box dimensions, and the number of Al atoms are listed in Table.I in the main text.

ii) Separate samples of liquid were created with all cross-sectional  $xy$  dimensions matching the crystal box. The dimension in  $z$ ,  $L_l$ , had the value of  $70\text{\AA}$ , which is large enough to avoid short-range forces (arises from density waves in the liquid) between two solid/liquid interface. Here we employed the equilibrium liquid density ( $\rho_l = 0.0309716\text{\AA}^{-3}$ , recorded in the supporting material of the Ref.3) and solubility predicted from the phase diagram,  $X_{\text{Al}} = 0.0016$ ,[4] under temperature at 750K and the pressure at 1 bar.

iii) The initial interface configurations were assembled by conjoining the solid Al and liquid Pb samples at their common cross-sections and applying periodic boundary conditions to the conglomerate. Initial separation distances between the crystal and the liquid samples were chosen to correspond with the minimum energy separation distance in the Al-Pb interaction energy.

iv) The solid/liquid systems were equilibrated using constant area, constant normal pressure ( $p_z=1$  bar), constant temperature MD simulations ( $Np_zAT$ ) for a long enough equilibration time of 50 ns, to make sure IL-IS coexistence at solid/liquid interface reaching structural and compositional equilibrium.

v) Finally, fixed volume  $NVT$  simulations were carried out, starting from the final configuration of the  $Np_zAT$  simulations, with  $L_z$  matches the average number from the  $Np_zAT$

simulations. The linear momentum for the solid was set to zero to avoid center of mass motion.

### C. Locating interfacial layer and an animation of the extracted monolayer

In the determination of the interfacial monoatomic layer as described in the methodology section and Fig.1 in the main text, one might note that the two peaks in the density profile do not overlap perfectly, which may be due to the size mismatch between the two elements. Current criterion of using the Al and Pb peak regime separately could avoid over-counting Al adatoms on top of the Al steps, or miscounting Pb interstitial in the Al steps.

Mov.S1 shows the same interfacial layer with IL-IS coexistence as presented in the Fig.2 of the the main text. The complete movie includes 350 frames covering a 0.7ns MD simulation, with time interval 2ps between neighboring frames. As in Fig.2 of the main text, the Al and Pb atoms are represented with circular plates and colored with the values of the order-parameter.

Our illustration indicates that the MD simulation is serving as a powerful tool aiding the experimental observation. The advanced TEM technique enables direct observations of the IL-IS coexistence at some types of solid/liquid interface;<sup>[5]</sup> however, these observations are usually limited in the side view aspect as presented in Fig.1 (a) in the main text, and achieving a *in situ* plan view of the interfacial layer is still challenging.

### D. Step positions

The following procedure is to quantitatively distinguish the interface crystalline phase from IL, in this process, We calculate the 2d structural order parameter<sup>[6]</sup> for each atom within the extracted interfacial layer,

$$\psi(i) = \left| \frac{1}{6Z_{2d}} \sum_{j=1}^{Z_{2d}} \sum_{\mathbf{q}_{\text{fcc}}} \exp(i\mathbf{q}_{\text{fcc}} \cdot \mathbf{r}_j) \right|^2, \quad (\text{S2})$$

where  $Z_{2d}$  is the number of atom  $j$  in the first neighbor shell surrounding atom  $i$ , within the monoatomic interfacial layer. This order parameter uses six reciprocal lattice vectors corresponding to the 6 lateral nearest neighbor directions in the fcc lattice.  $\exp(i\mathbf{q}_{\text{fcc}} \cdot \mathbf{r}_{\text{fcc}}) = 1$  if the atom is in the perfect fcc Al lattice at 750K. If atom  $i$  is in liquid phase then  $\psi(i)$  is

very close to 0. Both Al and Pb atoms were investigated, for those atoms close to the box boundary, its neighbor should be counted in the neighbor periodic box image.

In order to determine the positions of the step-edges, the whole interfacial layer was coarse-grained into  $m$  strips along the step direction ( $[10\bar{1}]$ ). The number of strips depends on the system size,  $m = L_y/\lambda$ ,  $\lambda = 1.44445\text{\AA}$ . Note that strips may go across the periodic boundary, which should be paid special attention to. In each strip, the best estimates of the step position is defined through a hyperbolic tangent function fitting of the order parameter profile across the step,  $(c_1 + c_2 \tanh(\frac{x^* - c_3}{c_4}))$ . Due to the small transverse size of the strip and the number of liquid phase atoms, nearly 30 percent of the initially attempted fittings fail and result in the step positions ( $\xi$ ) in those strips being undefined. A solution to circumvent this problem is to carry out two additional passes over the failed fittings. In the first pass, a hyperbolic tangent function  $(c_1 + c_2 \tanh(\frac{x^* - c_3}{W}))$  was employed to fit the order parameter profile in all the failure cases again,  $W$  is a constant equals to the average of all  $c_4$  values successfully obtained in the initially attempted fittings, under an assumption that the structural order profiles in all strips have similar width. In the second pass, the values of  $\xi$  at the remaining strips are interpolated from those values of their nearest neighbor strips.

Tab. S I. The step stiffness (free energy) measured from the capillary fluctuation spectra. Results obtained from MD simulation of the in-plane capillary fluctuations of a single step within the faceted Al(111)/Pb(*l*) interface at 750K and 1 bar. Data for eleven different system sizes are summarized. Error bars in parentheses represent 95% confidence intervals on the last digit(s).

| ID   | A      | B     | C      | D      | E     | F     | G     | H     | I     | J      | K     |
|--|--------|-------|--------|--------|-------|-------|-------|-------|-------|--------|-------|
| $\gamma_{\text{st}} = \bar{\gamma}_{\text{st}}(10^{-10}\text{mJ/m})$ | 75(13) | 86(8) | 83(10) | 72(12) | 87(8) | 69(7) | 79(6) | 79(8) | 74(9) | 72(10) | 86(9) |

## SECTION S2. SUPPORTING INFORMATION OF STEP FLUCTUATIONS AND STEP FREE ENERGY CALCULATION

### A. Supporting data: Al(111)/Pb(*l*) interfacial step free energy

The calculated data of  $\gamma_{\text{st}}$  (or  $\bar{\gamma}_{\text{st}}$ ) are listed in the Table.SI.

The fitting functions employed in Fig.4 (c) in the main text are listed as follows:

$$\begin{aligned} \bar{\gamma}_{\text{st}}(1/L_y) &= 65 + 1865 \times (1/L_y), && \text{linear} \\ \bar{\gamma}_{\text{st}}(1/L_y) &= 64 + 2813 \times (1/L_y) - 105640 \times (1/L_y)^2, && \text{quadratic} \\ \bar{\gamma}_{\text{st}}(1/L_y) &= 67 + 1757 \times (1/L_y) - 2954650 \times (1/L_y)^3, && \text{cubic} \end{aligned}$$

### B. Amplitude autocorrelation function

Representative plots of  $C_q(t)$  for six selected fluctuation wave vectors in system D, are shown in Fig.S2. From these results, we measure the relaxation times  $\tau_q$  for each fluctuation mode, which are presented in Fig.3(a) in the main text.

### C. Equilibrium island shape at Al(111)/Pb(*l*) interface

A non-negligible anisotropy in the step free energy is quite normal and sometimes the degree of the anisotropy can reach a very large value, *e.g.*, STM measurement of the of equilibrium shape of vacancy island on (111) Pt surface reported a degree of 15% in the anisotropy.[2] For the current study, there is no information yet available about the

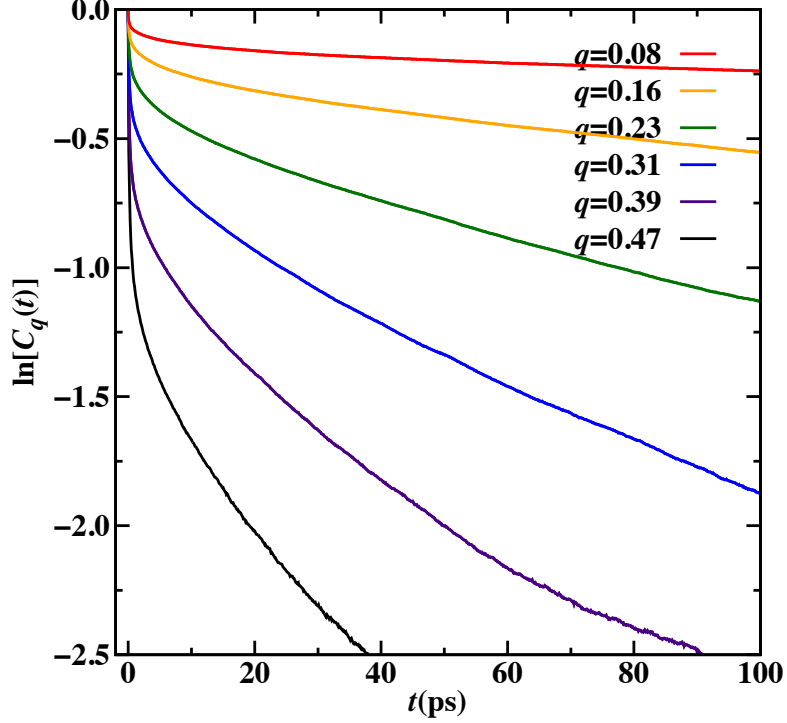


Fig. S 2. Step fluctuation amplitude autocorrelation functions for six wavevectors of system D. Calculations use time-dependent Fourier amplitudes of steps positions and Eq.2 in the main text.

anisotropy of  $\gamma_{st}$  for the steps in Al(111)/Pb(*l*) interfaces. Therefore, we carry out an independent island shape study to check the anisotropy and calculate the step free energy, using the minimum curvature analysis proposed by Giesen et al.[7] The study is designed for demonstrating the equilibrium shape of a solid island on liquid terrace, or a liquid island on solid terrace, within the solid/liquid interface. To avoid possible kinetic barriers preventing the island shape from reaching its equilibrium, two kinds of initial configurations of the liquid island on solid terrace are chosen, hexagonal (shown in Fig.S3) and circular shape (see in Fig.S4). The radius of the circular terrace or the circumradius of the hexagonal terrace are both equal to 30Å.

A sample of bulk fcc Al with sizes 120Å×120Å×80Å was prepared with the crystallographic orientations of the fcc sample arranged as  $[10\bar{1}]$ ,  $[\bar{1}2\bar{1}]$ , and  $[111]$ , corresponding to the  $x$ ,  $y$  and  $z$  axes, respectively. Starting from the center of the  $xy$  plane, based on the circular or hexagonal shapes, a portion of Al atoms in both the terminal layers of the solid

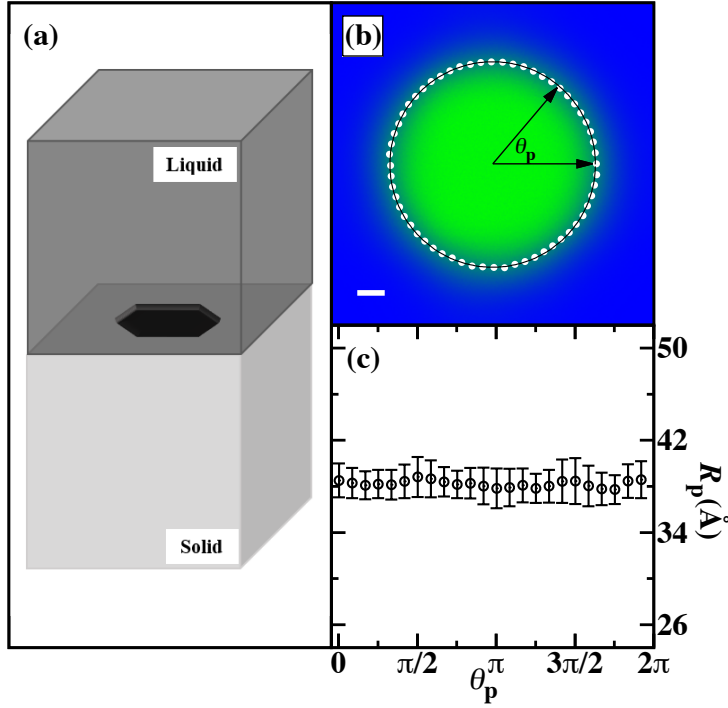


Fig. S 3. (a) Schematic diagram of the interfacial 2d island system, a hexagonal liquid Pb island in solid Al terrace as the initial configuration.  $T=750\text{K}$ ,  $p_z=1$  bar. (b) Density contour map (averaged over 1,260,000 configurations, two interfaces and 6 replica runs) and the coarse-grained outline for the 2d liquid island in Al(111)/Pb(*l*) interface at 750K. The shape outline is represented with white discs. Solid line is fitted to a circle. Scale bar 1nm. Color-scale of the plot for the area density is restricted to a range between 0 and  $0.13\text{\AA}^{-2}$ . (c) Radius along the island perimeter  $R_p$  as a function of angular directions  $\theta_p$ , error bars represent 95% confidence intervals estimated from statistical average.

sample are removed to make a solid terrace. We conjoin a sample of liquid Pb which has the same size as the solid sample together with the solid sample to form two solid/liquid interfaces under periodic boundary conditions. The equilibrium state of the solid/liquid interfaces, both in structural and compositional equilibration, are obtained with the same technique described in Ref.8. In the final equilibrium state, 6 replica *NVT* MD simulations last for 210ns each, with time-step of 2fs, and totally record 1,260,000 MD trajectories for the following analysis.

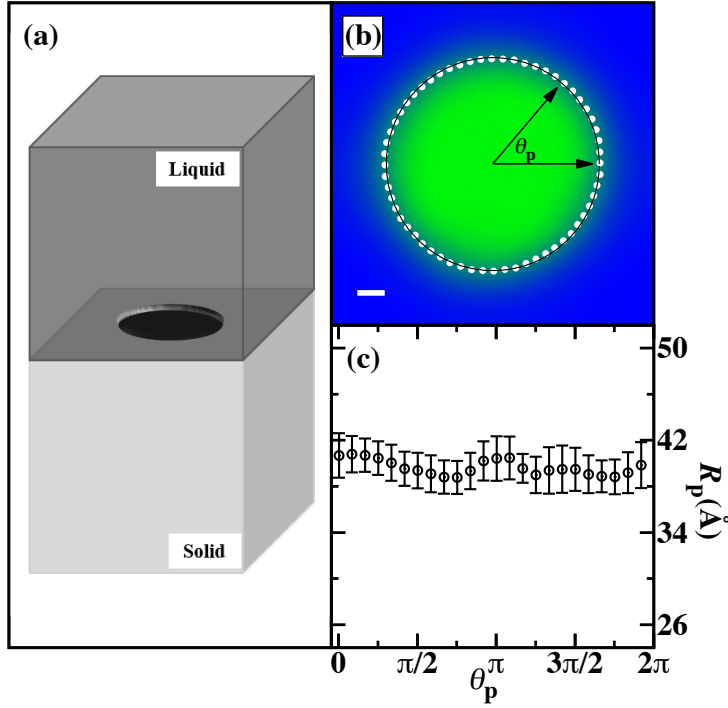


Fig. S 4. (a) Schematic diagram of the interfacial 2d island system, a circular liquid Pb island in solid Al terrace as the initial configuration.  $T=750\text{K}$ ,  $p_z=1$  bar. (b) Density contour map (averaged over 1,260,000 configurations, two interfaces and 6 replica runs) and the coarse-grained outline for the 2d liquid island in Al(111)/Pb(*l*) interface at 750K. The shape outline is represented with white discs. Solid line is fitted to a circle. Scale bar 1nm. Color-scale of the plot for the area density is restricted to a range between 0 and  $0.13\text{\AA}^{-2}$ . (c) Radius along the island perimeter  $R_p$  as a function of angular directions  $\theta_p$ , error bars represent 95% confidence intervals estimated from statistical average.

To extract the plan-view of the island-terrace configurations, the interfacial layer was determined from the mean density profiles as described in the main text. The Fig.S5 presents snapshot of a typical instantaneous in-plane liquid island-solid terrace coexistence in the interfacial layer. The atoms are color coded based on the order parameter defined above. It is shown that the instantaneous shapes of the island are complicated and deviate from a perfect circular geometry with a rough step structure. However, no clear “overhangs” at the boundaries are found in current simulations.

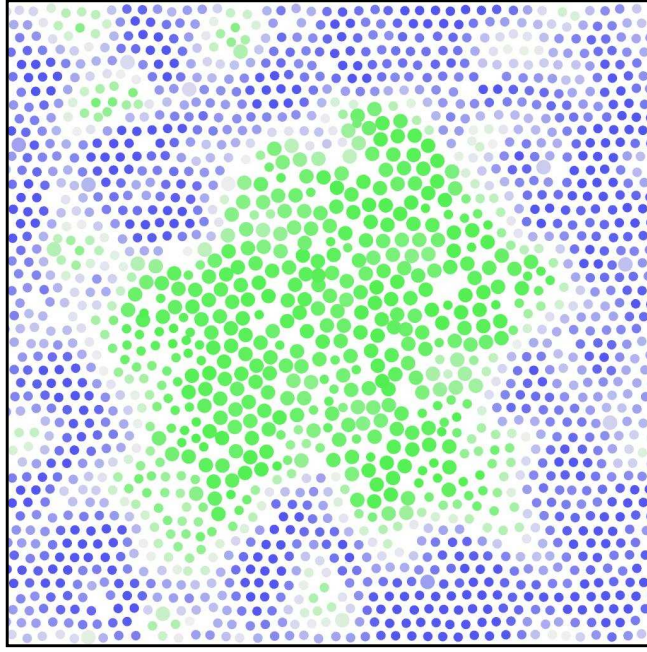


Fig. S 5. A snapshot of the interfacial island (plan view). The Al and Pb atoms are represented with the same size symbols and colored based on the order-parameter values same as Fig.2 in the main text. Rough type step structure without clear “overhangs” at the step-edges is shown.

We employ analysis on the average two-dimensional density map,  $\langle \rho_{xy}(\mathbf{r}) \rangle$ , to produce a precise equilibrium island shape. The average includes liquid phase particles found in the interfacial monoatomic layer, which is partitioned into a  $200 \times 200$   $xy$  grid. Note that, the 2d island was found to drift randomly during the equilibrium MD simulation time. In order to avoid misestimation of the equilibrium shape generated by this island drift (plotted in the panel (a) of Fig.S6 showing the time evolution of center of mass (COM) of the island), we have aligned the COM of liquid Pb atoms in the calculation of the  $\langle \rho_{xy}(\mathbf{r}) \rangle$ . The time-averaged particle density is calculated in each grid, by averaging over 10,000 configurations. The entire 720,000 configurations give 72 sub-averaged 2d density maps. Three representative sub-averaged density contour maps are shown in Fig.S6. The panel (b) in Fig.S3 and in Fig.S4 as shown the contour plots of the  $\langle \rho_{xy}(\mathbf{r}) \rangle$  for the average over all 720,000 configurations.

In order to quantitatively measure the shape of the equilibrium island, the island shape

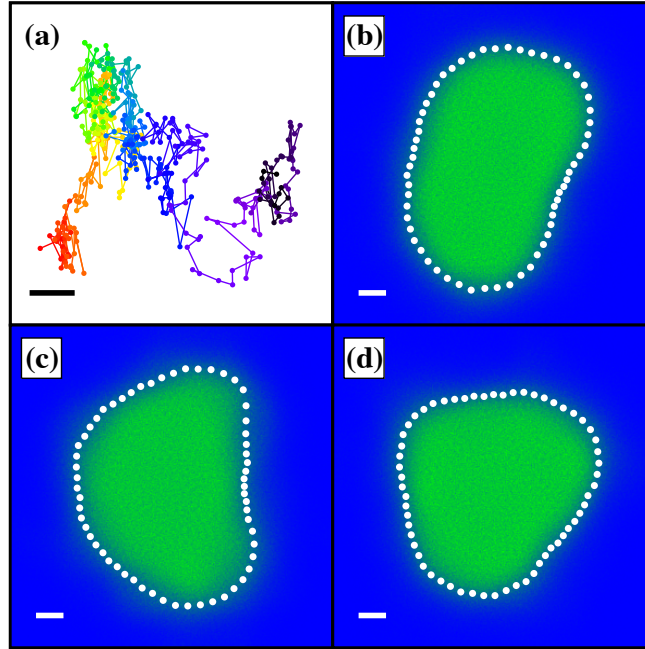


Fig. S 6. (a) Trajectories of island COM 2d motion in the Al(111)/Pb(*l*) interfacial layer, recorded over the same time period of 210ns, each step is 500ps. The time variable is labeled with a rainbow color scale. 750K. (b)(c)(d) show three selected sub-averaged density contour maps and the coarse-grained outlines for the islands. Scale bars are 1nm.

is outlined by defining the step-edge positions at the equimolar dividing surfaces. From the COM of the island, the sub-averaged density contour map is coarse-grained into sectors, each along a radial line in a direction  $\theta_p$ . In each sector, the density distribution is treating as a profile along such radial direction, and we employ a hyperbolic tangent function to fit such radial order-parameter density profile and calculate the equimolar dividing surface.[9] The procedure is repeated for 360 equally distributed angular directions  $\theta_p$ , the outline of the sub-averaged island shape and the radius along the outline ( $R_p$ ) as a function of  $\theta$  are measured. The three sub-average outlines (with open circles) plotted in Fig.S6 indicate that fluctuation of the island shape is significant, but the full time-averaged island shape outlines appear to be almost perfectly circular and are well fitted with circular functions, as shown in Panel (c) of Fig.S3 and Fig.S4. Alternatively, within statistical uncertainties, the radii

along the island perimeter are identical. These statistically meaningful results lead us to conclude that  $\gamma_{st}$  is isotropic and  $\gamma_{st} = \bar{\gamma}_{st}$  for the solid/liquid interfacial step systems in the current study.

SECTION S3. SUPPORTING INFORMATION OF THE IN-PLANE CHARACTERIZATION

A. In-plane structure of IS and IL at Al(111)/Pb(*l*)

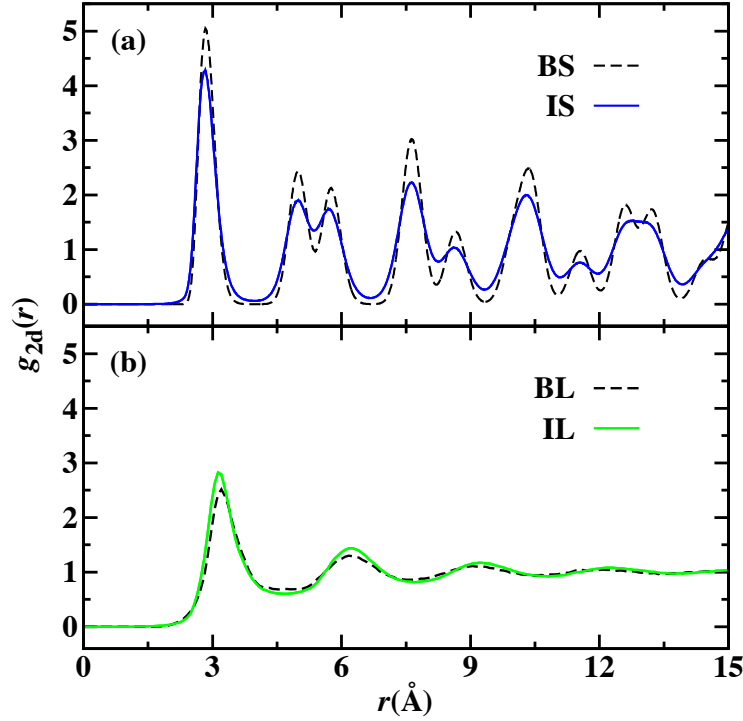


Fig. S 7. Two-dimensional RDF of IS and IL Al(111)/Pb(*l*) interface,  $T=750\text{K}$ . Solid lines in panel (a) and (b) represent results of IS and IL, respectively. These are compared with the two-dimensional RDF calculated for bulk solid (BS) Al and bulk liquid (BL) Pb at the same temperature, represented with dashed lines.

Structural analyses are carried out to characterize the in-plane structural ordering in IS and IL. In all analysis, we choose the “bulk” part of IS and IL as the regimes that are  $20\text{\AA}$  away from the instantaneous step-edge positions  $\xi(y_i)$ , and the calculation average over 50000 configurations and two interfaces. The in-plane structural ordering is examined by the two-dimensional radial distribution function (RDF)  $g_{2d}(r)$  for particle-particle pairs. For comparison, we have also carried out two-dimensional RDF analysis for the bulk solid and bulk liquid at 750K, using the layer width  $\delta z^*$  same as the interfacial layer. Fig.S7 shows

Tab. S II.  $\tilde{X}_{\text{Al}}^l$  and  $\tilde{X}_{\text{Pb}}^s$ . Error bars in parentheses represent 95% confidence intervals on the last digit(s) shown. Data for eight different system sizes at 750K are summarized.

| ID                            | A      | B      | C      | D      | E      | F      | G      | H      |
|-------------------------------|--------|--------|--------|--------|--------|--------|--------|--------|
| $\tilde{X}_{\text{Al}}^l(\%)$ | 22(5)  | 19(1)  | 19(2)  | 20(4)  | 20(2)  | 20(2)  | 20(1)  | 21(5)  |
| $\tilde{X}_{\text{Pb}}^s(\%)$ | 1.8(2) | 1.4(1) | 1.6(2) | 2.0(4) | 1.6(2) | 1.9(2) | 1.8(2) | 1.5(3) |

the calculated two-dimensional RDF for the interface liquid Pb and bulk liquid Pb phases. In the  $g_{2d}(r)$  of IS and IL, the peaks are commensurate with those of their respective bulk liquid phases. There are small differences in terms of the amplitude and width of the  $g_{2d}(r)$  peaks, which could be due to the increment of the Al-Pb intermixing.

### B. Supporting data: $\tilde{X}_{\text{Al}}^l$ and $\tilde{X}_{\text{Pb}}^s$

Table.SII lists  $\tilde{X}_{\text{Pb}}^l$  and  $\tilde{X}_{\text{Al}}^l$  calculated from eight system sizes in current study, within the statistical uncertainties, the data are nearly identical, indicating the abnormal increase of the miscibility (comparing with the bulk phase) in IS and IL is robust, independent of the simulation dimensions.

### C. Coarse-scaled interfacial profiles for 750K Al(111)/Pb(*l*)

The coarse-scaled Al(111)/Pb(*l*) interfacial density, concentration, potential energy, pressure components profiles are calculated following the method described in Ref.8, for the system size D. In Fig.S8 we plot these profiles as functions of the distance to the Gibbs dividing surface, defined as the interfacial excess of Al atoms is equal to zero. Bulk phases thermodynamic parameters listed in Table.II in the main text are extracted from bulk region of these profiles. For example, the pressure profiles across the equilibrium Al(111)/Pb(*l*) interface, are found to be uniformly distributed in both bulk phases, with  $p^s = p^l = 1$  bar (under ambient conditions), and with only exhibiting variations in the vicinity of the interface. The stress in the 3d bulk solid and bulk liquid is zero due to the hydrostatic balance condition and the two bulk phases are in mechanical equilibrium.

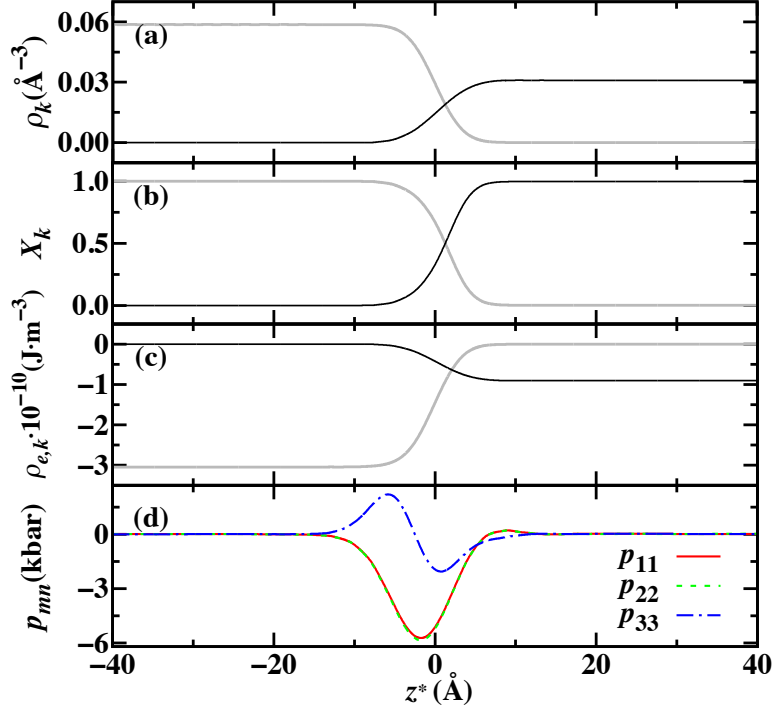


Fig. S 8. Coarse-scaled density (a), coarse-scaled concentration (b), coarse-scaled potential energy (c) and pressure components (d) profiles across the Al(111)/Pb(*l*) interface (system size D). The lines in dark and light gray in (a)(b)(c) represent properties for Pb and Al, respectively. Different line types stand for the three pressure components in (d). Zero point ( $z^*$  axis) in corresponding to the Gibbs Dividing Surface, chosen as the interfacial excess of Al atoms equals to zero.

- 
- [1] D. Buta, M. Asta, J. J. Hoyt, Kinetic coefficient of steps at the si(111) crystal-melt interface from molecular dynamics simulations, *The Journal of Chemical Physics* 127 (7). [doi:10.1063/1.2754682](https://doi.org/10.1063/1.2754682).
- [2] J. Ikonov, K. Starbova, H. Ibach, M. Giesen, Measurement of step and kink energies and of the step-edge stiffness from island studies on pt(111), *Phys. Rev. B* 75 (2007) 245411. [doi:10.1103/PhysRevB.75.245411](https://doi.org/10.1103/PhysRevB.75.245411).
- [3] Y. Yang, M. Asta, B. B. Laird, Solid-liquid interfacial premelting, *Phys. Rev. Lett.* 110 (2013) 096102. [doi:10.1103/PhysRevLett.110.096102](https://doi.org/10.1103/PhysRevLett.110.096102).

- [4] A. Landa, P. Wynblatt, D. Siegel, J. Adams, O. Mryasov, X.-Y. Liu, Development of glue-type potentials for the alpb system: phase diagram calculation, *Acta Materialia* 48 (8) (2000) 1753 – 1761. doi:10.1016/S1359-6454(00)00002-1.
- [5] S. H. Oh, M. F. Chisholm, Y. Kauffmann, W. D. Kaplan, W. Luo, M. Rühle, C. Scheu, Oscillatory mass transport in vapor-liquid-solid growth of sapphire nanowires, *Science* 330 (6003) (2010) 489–493. doi:10.1126/science.1190596.
- [6] J. R. Morris, Complete mapping of the anisotropic free energy of the crystal-melt interface in al, *Phys. Rev. B* 66 (2002) 144104. doi:10.1103/PhysRevB.66.144104.
- [7] M. Giesen, C. Steimer, H. Ibach, What does one learn from equilibrium shapes of two-dimensional islands on surfaces?, *Surface Science* 471 (13) (2001) 80 – 100. doi:10.1016/S0039-6028(00)00888-8.
- [8] Y. Yang, D. L. Olmsted, M. Asta, B. B. Laird, Atomistic characterization of the chemically heterogeneous alpb solidliquid interface, *Acta Materialia* 60 (12) (2012) 4960 – 4971. doi:10.1016/j.actamat.2012.05.016.
- [9] T. Werder, J. H. Walther, R. L. Jaffe, T. Halicioglu, P. Koumoutsakos, On the watercarbon interaction for use in molecular dynamics simulations of graphite and carbon nanotubes, *The Journal of Physical Chemistry B* 107 (6) (2003) 1345–1352. doi:10.1021/jp0268112.